Contents lists available at ScienceDirect

# Applied Catalysis B: Environmental

journal homepage: www.elsevier.com/locate/apcatb

# Evaluation of MgO as a promoter for the hydrogenation of $CO_2$ to long-chain hydrocarbons over Fe-based catalysts

Sheraz Ahmed [a], Muhammad Irshad [b], Wonjoong Yoon [b], Neha Karanwal [a], Junjung Rohmat Sugiarto [a], Muhammad Kashif Khan [b,c,*,1], Soek Ki Kim [d], Jaehoon Kim [a,b,c,**,1]

[a] SKKU Advanced Institute of Nano Technology (SAINT), 2066, Seobu-Ro, Jangan-Gu, Suwon, Gyeong Gi-Do 16419, Republic of Korea
[b] School of Chemical Engineering, Sungkyunkwan University, 2066, Seobu-Ro, Jangan-Gu, Suwon, Gyeong Gi-Do 16419, Republic of Korea
[c] School of Mechanical Engineering, Sungkyunkwan University, 2066, Seobu-Ro, Jangan-Gu, Suwon, Gyeong Gi-Do 16419, Republic of Korea
[d] Department of Chemical Engineering, Ajou University, Suwon 16499, Republic of Korea

## ARTICLE INFO

## ABSTRACT

Thermocatalytic conversion of $CO_2$ into liquid fuels and chemicals is a promising approach to mitigate global warming. Although, the $CO_2$ conversion and long-chain hydrocarbon selectivity are highly dependent on the choice of metal-oxide promoter, but role of the promoter remains unclear. Herein, the role of MgO as a promoter for an Fe-based catalyst was investigated. Bimetallic Na-FeMgO$_x$ catalyst exhibited a high $C_{5+}$ yield of 25.1% with a $CO_2$ conversion of 49.1% at the early stage of the reaction. The presence of MgO facilitates the reduction of Fe oxides and formation of oxygen vacancies by transferring electrons to Fe-based phases. In addition, at the early stage of reaction, the decoration of the Mg oxide surface with nanosized $\chi$-Fe$_5$C$_2$ enhances the $C_{5+}$ yield. However, the progressive transformation of MgO to MgCO$_3$ during $CO_2$ conversion deactivates the Na-FeMgO$_x$ catalyst. A detailed deactivation mechanism is also discussed.

## 1. Introduction

The concentration of $CO_2$ in the atmosphere has increased significantly since the start of the last century due to the extensive use of fossil fuel, resulting in adverse effects, such as ocean acidification, global climate change, and unexpected changes in the ecosystem [1–3]. To mitigate the detrimental effects associated with anthropogenic $CO_2$ emissions, various approaches based on thermochemical, biological, and electrochemical conversion techniques have been proposed [4]. Among these, the direct conversion of $CO_2$ to fuels and value-added chemicals via the reverse–water–gas shift (RWGS) reaction followed by C–C coupling via Fischer–Tropsch synthesis (FTS) is considered one of the most promising techniques [5,6]. Catalytic hydrogenation of $CO_2$ is considered a versatile route for synthesizing a range of products, including monocarboxylic acids, alcohols, light olefins, long-chain hydrocarbons, and aromatics [7–14].

The high RWGS and FTS activity associated with alkali metal-promoted Fe-based catalysts make them favorable catalyst candidates for the direct conversion of $CO_2$ to liquid fuel-range hydrocarbons ($C_{5+}$) [5,6]. As in the case of typical syngas conversion, direct $CO_2$ hydrogenation over an Fe-based catalyst requires high temperature (300–400 °C), which makes Fe nanoparticles highly susceptible to sintering [15]. In addition, sole alkali-promoted Fe catalysts without metal-oxide promoters (for example, Na–Fe$_3$O$_4$) exhibited relatively low $C_{5+}$ yields (0.8–13.4%) [16,17], when including CO, Table S1, Fig. S1a). To suppress particle agglomeration and increase $C_{5+}$ yields, the incorporation of a metal oxide (e.g., amorphous AlO$_x$ [12], ZnO [15], TiO$_2$ [18], ZrO$_2$ [19], or SiO$_2$ [20]) as a support or promoter and zeolite as a C–C coupling agent [21–23] has been proposed. However, the specific role of metal oxide as a structural or electronic promoter is still unclear. In the case of zeolites, their low hydrothermal stability and undesirable coking of the micropores, which eventually deactivate the composite catalyst, should be carefully addressed [14].

Since the early 1990 s, Mg-supported or Mg-promoted Fe-based

catalysts have been considered as promising catalyst systems for the synthesis of light olefins ($C_2^=$–$C_4^=$) by syngas conversion [24–36]. In the previous literature, "Mg-promotion" has been used as a general term to describe promotion by metallic $Mg^0$, $Mg^{2+}$ ions, and partially or fully oxidized $MgO_x$ ($0 < x \leq 1$). Considering the different physicochemical properties and electronic structures of $Mg^0$, $Mg^{2+}$, and $MgO_x$, their roles as promoters in syngas conversion probably differ; this could explain the long-running debate on the potential role of "Mg" as a promotor in syngas conversion. In addition, the changes in the chemical environment of Mg due to its conversion to $MgCO_3$ and $Mg(OH)_2$ (by reactions with $CO_2$ and $H_2O$, respectively during syngas conversion [26]), should be carefully investigated to elucidate its role as a promotor. For example, in Co-based catalysts, metallic Mg and partially oxidized $MgO_x$ ($x < 1$) promote dissociative adsorption of CO, while fully oxidized MgO retards this process [37–39]. In contrast, it was demonstrated that the presence of MgO in the Co catalyst increases CO adsorption at interfacial sites, increases Co dispersion, and suppresses $CO_2$ formation [40]. During syngas conversion, the presence of MgO suppresses the water–gas–shift (WGS) reaction [28,29], while in some cases, the WGS reaction is enhanced [31,35] or marginally changed [33,34]. Under the assumption that the MgO structure is maintained during syngas conversion, its beneficial role as an electronic promoter includes weakening adsorbed C–O bonds (by facilitating the back-bonding of metal electrons to the antibonding orbitals of CO) and decreasing the dissociative adsorption of $H_2$, which eventually decreases the selectivity of $CH_4$ and increases the selectivity of olefins in the product streams [26,31,32,34,36]. In addition, the role of MgO as a structural promoter was reported; the presence of MgO suppressed the growth of Fe-oxide particles, which facilitates the formation of Fe carbides and enhances the $C_{5+}$ yields [28]. In contrast, no significant promotional effect of MgO was observed for KCuFe/mesoporous $Al_2O_3$ catalyst [33]. In addition, the enhanced adsorption of $H_2$ and suppression of Fe-carbide formation were observed for a $FeMnMgO_x$ catalyst [35]. Although the role of MgO in promoting syngas conversion is still unclear, some MgO-promoted Fe catalysts enhance the amount of $C_2^=$–$C_4^=$ in the product stream. In addition to promoting syngas conversion, MgO can be applied as an electronic or structural promoter in the high-yield synthesis of $C_{5+}$ via direct $CO_2$ hydrogenation using the combined RWGS and FTS processes. However, the MgO-promoted Fe catalysts have rarely been investigated. In addition, previously, the correlation between structure and activity, as well as the deactivation mechanism during long-term reactions, has rarely been investigated. Most previous studies presented data for less than 200 h-on stream reaction (Fig. S1b), which is far less than what is required in typical industrial settings. Although understanding the potential deactivation mechanisms during long-term reactions is a prerequisite for developing industry-relevant catalysts, it is challenging to do so due to the lack of research in this area.

In this study, we investigate the role of MgO in Fe catalysts for the direct synthesis of $C_{5+}$ through $CO_2$ conversion. A series of Na–FeMgO$_x$ catalysts with varying ratios of Fe and Mg (Na–FeMgO$_x$-*y* where *y* = Fe/ [Fe + Mg] × 10) were synthesized by a co-precipitation method. The Na–FeMgO$_x$-*y* catalysts were tested at various reaction conditions, such as temperature, pressure, space velocity, and $CO_2$/$H_2$ ratio. Under optimal conditions, an unprecedently high $C_{5+}$ yield of 25.1% was achieved over the Na–FeMgO$_x$-5 catalyst (Table S1, Fig. S1a). The transformation of MgO to $MgCO_3$ during $CO_2$ hydrogenation, the promotional effect of MgO, and deactivation mechanisms are discussed here.

## 2. Materials and methods

### 2.1. Materials

Iron (III) nitrate nonahydrate (Fe(NO$_3$)$_3$·9 H$_2$O, 99.9%), , magnesium (II) nitrate hexahydrate (Mg(NO$_3$)$_2$·6 H$_2$O, 99.9%), sodium hydroxide (NaOH, >98%), 1-octene (99%), and dodecane (99%) were

purchased from Alfa Aesar (USA). Sodium carbonate (Na$_2$CO$_3$, 99.98%), hydrochloric acid (HCl, 37%), and ammonium carbonate ((NH$_4$)$_2$CO$_3$, $\geq$ 30.0% NH$_3$ basis) were acquired from Sigma–Aldrich (USA). Dichloromethane (DCM, >99.9%) and methanol (99.9%) were purchased from Daejung Chemicals and Metals (South Korea). Ethanol (99.9%) was obtained from Honeywell Burdick & Jackson (USA). High-purity $CO_2$ (99.995%), $H_2$ (99.999%), $N_2$ (99.999%), He (99.999%), Ar (99.999%), and 5% CO/He gases were purchased from JC Gas Company (South Korea). Distilled and deionized (DDI) water was produced using an EXL® 7 S Analysis water purification system equipped with a 0.22 μm filter (Vivagen Co., Ltd., South Korea).

### 2.2. Catalyst preparation

The Na–FeMgO$_x$-*y* catalysts were synthesized by the co-precipitation method using various ratios of iron and magnesium salts. For example, for the synthesis of Na–FeMgO$_x$-5, 10 g of Fe(NO$_3$)$_3$·9 H$_2$O and 10 g of Mg(NO$_3$)$_2$·6 H$_2$O were dissolved in 100 mL of DDI water. A solution containing 13.52 g of Na$_2$CO$_3$ and 128 mL of DDI water was prepared as a precipitant. The aqueous precipitant solution was added dropwise to the iron (III) and magnesium (II) nitrate aqueous solution under stirring at 85 °C with maintaining a pH of 8.5. After the addition of the precipitant, the solution was stirred at 85 °C for 14 h; during the stirring, a brown precipitate was formed. After stirring and natural cooling, the suspension was aged for 6 h at 25 ± 2 °C. The precipitate settled at the bottom of a beaker was collected by filtering using a Whatman #2 filter paper. The precipitate on the filter paper was washed with 300 mL of DDI water and then dried in a convection oven at 80 °C for 14 h. The dried precipitate was then calcined at 600 °C for 6 h under static air conditions. The ingredients for the synthesis of other Na–FeMgO$_x$-*y* catalysts with varying *y* are listed in Table 1. The Na–FeMgO$_x$-*y* catalysts were reduced ex-situ at 450 °C for 10 h under a 50 mL min$^{-1}$ flow of 5% H$_2$/Ar and then used for further characterization experiments.

For comparison, sodium-promoted iron oxide (Na–Fe$_2$O$_3$) was synthesized. Briefly, 20.0 g of Fe (NO$_3$)$_2$·9 H$_2$O was dissolved in 150 mL of DDI water under magnetic stirring to form a clear solution. A solution containing 10.8 g of Na$_2$CO$_3$ and 109.5 mL of DDI water was prepared as a precipitant. The precipitant solution was added dropwise to the iron nitrate solution under magnetic stirring at 85 °C with maintaining a pH of 8.5. After adding the precipitant, the solution was stirred at 85 °C for 14 h, and brown precipitates were formed during the stirring. After stirring and natural cooling, the suspension was aged for 6 h at 25 ± 2 °C. The precipitate settled at the bottom was collected by filtering using a Whatman #2 filter paper, and then dried in a convection oven at 80 °C for 14 h. The dried precipitates were then calcined at 600 °C for 6 h under static air conditions.

**Table 1**
Formulations used in the synthesis of Na–FeMgO$_x$-*y* catalysts.

| Catalyst | Fe (NO$_3$)$_3$·9 H$_2$O (g) | Mg (NO$_3$)$_2$·6 H$_2$O (g) | Na$_2$CO$_3$ (g) | DDI water (g) |
|---|---|---|---|---|
| Na–MgO | 0 | 20 | 8.3 | 78.0 |
| Na–FeMgO$_x$-1 | 2 | 18 | 8.0 | 75.0 |
| Na–FeMgO$_x$-2 | 4 | 16 | 15.3 | 72.3 |
| Na–FeMgO$_x$-5 | 10 | 10 | 13.5 | 128.0 |
| Na–FeMgO$_x$-7 | 14 | 6 | 6.2 | 58.1 |
| Na–FeMgO$_x$-9 | 18 | 2 | 11.1 | 104.7 |
| Na–Fe$_2$O$_3$ | 20 | 0 | 10.8 | 109.5 |

## 2.3. Catalyst characterization

The crystallinity of calcined, reduced, and spent catalysts was measured using X-ray diffraction (XRD; D/Max–2500 V/PC, Rigaku, Japan) with a Cu-Kα radiation source ($\lambda = 1.5418$ Å) operated at 40 kV and 50 mA. The XRD patterns were collected over the $2\theta$ range of 20–85° with a step size of 0.02°. The morphologies of the Na–FeMgO$_x$-$y$ catalysts were analyzed using scanning transmission electron microscopy (STEM; TitanTM 80–300, FEI, USA) and high-resolution transmission electron microscope (HR–TEM; FEI Talos F200X, USA) equipped with an energy-dispersive X-ray spectroscopy system (EDS; Super-X EDX, Bruker, USA) operated at 200 keV. The textural properties of the catalysts were evaluated by collecting their $N_2$ adsorption–desorption isotherm profiles at − 196 °C using a Belsorp-mini II instrument (BEL Inc., Japan). The specific surface areas of the catalysts were calculated using the multipoint Brunauer–Emmett–Teller (BET) method and the pore-size distributions were calculated from Barrett–Joyner–Halenda (BJH) plots. Prior to the measurements, the catalysts were pretreated under vacuum at 120 °C for 8 h to eliminate moisture and other volatile organic species. The contents of each element in the Na–FeMgO$_x$-$y$ catalysts were analyzed using inductively coupled plasma–optical emission spectroscopy (ICP–OES, Optima 7300 V, PerkinElmer, USA).

The temperature-programmed reduction of hydrogen (H$_2$–TPR) was performed to observe the reduction behavior of the catalysts. Prior to measurement, the calcined catalyst (50 mg) was heated at 250 °C for 1 h under an Ar atmosphere to remove adsorbed water and other volatile impurities. After naturally cooling to 50 °C, the catalyst was then flushed with Ar for 30 min. The temperature was then increased to 900 °C at a ramp rate of 10 °C min$^{-1}$ under a 30 mL min$^{-1}$ flow of 5% H$_2$/Ar to reduce the catalyst. Temperature-programmed desorption of hydrogen (H$_2$–TPD) was conducted using a BELCAT-M instrument (BEL Inc., Japan). Typically, 50 mg of pre-reduced catalyst was added to a quartz sample tube. The sample tube was heated to 450 °C at a ramp rate of 5 °C min$^{-1}$ under a flow of 30 mL min$^{-1}$ of 5% H$_2$/Ar. Catalyst reduction was performed at 450 °C for 2 h. Then, the sample tube was cooled to 50 °C and the catalyst was completely saturated with 5% H$_2$/Ar at a flow rate of 30 mL min$^{-1}$ for 30 min. Subsequently, the entire system was purged with ultra-high purity Ar (30 mL min$^{-1}$ for 1 h) to remove physically adsorbed hydrogen molecules. The sample tube was then heated to 950 °C at a ramp rate of 5 °C min$^{-1}$ under an Ar gas flow (30 mL min$^{-1}$) for the H$_2$–TPD analysis. Temperature-programmed desorption of carbon dioxide (CO$_2$–TPD) was performed to determine the basicity of the catalyst. The pre-reduced catalyst was further reduced for 30 min under pure 5% H$_2$/Ar at 450 °C and flushed with helium for 15 min. Then, the sample tube was naturally cooled and a flow of CO$_2$ (30 mL min$^{-1}$) was supplied to the sample tube for 1 h. The physiosorbed CO$_2$ molecules were then removed by purging the whole system with He (30 mL min$^{-1}$ for 15 min). Finally, CO$_2$ desorption measurements were performed by increasing temperature to 950 °C at a heating rate of 10 °C min$^{-1}$ under a 30 mL min$^{-1}$ flow of He. Temperature-programmed oxidation (O$_2$-TPO) of spent catalysts was performed to examine the presence of χ-Fe$_5$C$_2$ and carbon. Prior to measurement, the spent catalyst (50 mg) was heated at 150 °C for 1 h under He atmosphere to remove adsorbed water and other volatile impurities. After naturally cooling to 50 °C, the catalyst was flushed with He for 30 min and temperature was then increased to 950 °C at a ramp rate of 10 °C min$^{-1}$ under a 30 mL min$^{-1}$ flow of 5% O$_2$/He to oxidize the catalyst.

X-ray photoelectron spectroscopy (XPS) of the calcined, reduced, and spent catalysts were performed using ESCALAB250Xi spectrometer (Thermo Scientific, UK). The characteristic C–C 1 s peak at 284.8 eV was used as a reference for calibrating the positions of all peaks. Fe K-edge X-ray absorption spectroscopy (XAS) was conducted at the 8 C beamline of the Pohang Accelerator Laboratory using a Si (111) double crystal monochromator in transmission mode. Reference spectra were collected simultaneously from a Fe foil for energy calibration. The extended X-ray absorption fine structure (EXAFS) and X-ray absorption near edge

structure (XANES) data were analyzed using the Athena/Artemis software package [41]. To emphasize the high-energy oscillations, the extracted EXAFS signal, $\chi(k)$, was weighted by $k^3$, and the Fourier transform was performed in the $k$-range of 3.0–11.0 Å using a Hanning window function to obtain the magnitude plot of the EXAFS spectrum in $R$-space. To investigate Fe phases in the reduced and spent Na–FeMgO$_x$-5 catalyst, $^{57}$Fe Mössbauer spectra were collected at room temperature. A radioactive cobalt ($^{57}$Co) source in a rhodium matrix was transferred in constant acceleration mode. The spectra were calibrated using the spectra obtained from an α-Fe foil. Data fittings was performed by assuming Lorentzian line-shape characteristics. To identify the different iron phases, three Mössbauer parameters (isomer shift, magnetic hyperfine field, and quadruple splitting) were used.

## 2.4. Catalyst evaluation

A continuous fixed-bed reactor comprising a stainless-steel reactor with an inner diameter of 10 mm, gas feed lines, and a condenser, was used to evaluate the catalysts for CO$_2$ hydrogenation. A detailed description of the reactor has been provided in our previous paper [12]. For a typical reaction, a mixture of calcined Na–FeMgO$_x$-$y$ catalyst (1 g) and silica (3 g, Fisher Chemicals, S/0365/60) as a thermal diluent was fixed in the middle of the reactor using quartz wool. Then, the Na–FeMgO$_x$-$y$ catalyst was reduced in situ at 450 °C under a H$_2$ flow (50 mL min$^{-1}$ and 3.5 MPa for 10 h). After reduction, the reactor was allowed to cool to the experimental set temperature (270–360 °C), and then a flow of H$_2$/CO$_2$ (3:1) was introduced to the reactor at 3.5 MPa. The product stream was passed through the condenser (maintained at 25 °C and a given reaction pressure) to liquify the produced hydrocarbons. The gas stream that was emitted from the condenser was directed toward an online refinery gas analyzer-gas chromatograph (RGA–GC, PerkinElmer Clarus 580 GC-Model Arnel 1115PPC, PerkinElmer, USA) to analyze the gas stream. The detailed procedure and specifications of the RGA–GC tests were given elsewhere [42].

The liquid products collected in the condenser were analyzed by gas chromatography-time-of-flight mass spectrometry (GC–TOF/MS). The model 7890 A GC and Pegasus HT TOF/MS instruments were manufactured by Agilent Technologies (USA) and LECO Corporation (USA), respectively. The details of the GC–TOF/MS are described elsewhere [12]. After the liquid product in the water phase was collected by liquid-liquid extraction with DCM, approximately 1 μL of the DCM solution was injected into a Rxi-5Sil-MS column (30 m × 0.25 mm × 0.25 μm, Restek, USA) in a split mode of 25:1. The injector and transfer line temperatures were set at 250 and 260 °C, respectively. The temperature of the column was maintained at 40 °C to initiate heating with a holding time of 2 min, and then the temperature was increased to 300 °C at a rate of 10 °C min$^{-1}$. Quantification analysis of the liquid product was performed using a GC equipped with a flame ionization detector (FID) and a Rxi-5 Sil-MS capillary column (30 m × 0.25 mm × 0.25 μm, Restek). Generally, 1 μL liquid product was injected into the GC column at a split ratio of 1:10. Both the inlet and detector temperatures were set to 250 °C. Initially, the column temperature was held at 50 °C for 2 min and then the temperature was increased from 50° to 250°C at a rate of 10 °C min$^{-1}$ and then held for 5 min before cooling to 50 °C. The FID response was quantitatively analyzed using an effective carbon number method with 1-octene and dodecane as standards for branched hydrocarbons and linear hydrocarbons, respectively. The quantification details were described elsewhere [12]. The aqueous phase collected from the liquid product, which contained oxygenated species (e.g., carboxylic acids, ketones, and alcohols) was analyzed by high-performance liquid chromatography (HPLC) using a Bio-Rad Animex HPX-87 H column (Bio-Rad, USA, 300 mm × 7.8 mm) with a UV-Vis detector ($\lambda = 220$ nm).

The distribution of gas and liquid hydrocarbons was expressed based on the carbon mole function. The typical carbon balance obtained in the catalyst test was in the range of 90–95% based on a 50 h on-stream reaction. The CO selectivity, CO$_2$ conversion, hydrocarbon selectivity,

hydrocarbon yield, and carbon balance were calculated using Eqs. (1)–(6) (all in mol% of C). In the subsequent equations, $CO_{out}$, $CO_{2in}$, and $CO_{2out}$ represent the mole fractions of CO at the outlet, $CO_2$ at the intlet, and $CO_2$ at the outlet, respectively.

$$CO\ selectivity = \frac{CO_{out}}{CO_{2in} - CO_{2out}} \times 100\% \tag{1}$$

$$CO_2\ conversion = \frac{CO_{2in} - CO_{2out}}{CO_{2in}} \times 100\% \tag{2}$$

$$\text{Hydrocarbon selectivity including } CO = \frac{\text{Moles } of\ C_i\ \text{hydrocarbon } \times\ i}{CO_{2in} - CO_{2out}} \times 100\% \tag{3}$$

$$\text{Hydrocarbon selectivity excluding } CO = \frac{\text{Moles } of\ C_i\ \text{hydrocarbon } \times\ i}{\sum_{i=1}^{n} \text{Moles } of\ C_i\ \text{hydrocarbons } \times\ i} \times 100\% \tag{4}$$

$$\text{Hydrocarbon } yield = \frac{\text{Selectivity of } all\ \text{the } HC's\ \text{including } CO \times CO_2\ \text{conversion}}{100} \tag{5}$$

$$\text{Carbon } balance = \frac{CO_{out} + \sum_{i=1}^{n=5} RGA - GC, C_iH_j + \sum_{i=1}^{n=5} HPLC, C_iH_jO_k + \sum_{i=6}^{n=19} GC - FID, C_iH_j}{CO_{2in}\ -\ CO_{2out}} \tag{6}$$

## 2.5. DFT simulation

DFT simulations were performed using the Material Studio 2022 package and CASTEP program [43]. The generalized gradient approximation method was applied with the Perdew-Burke-Ernzerh of exchange correlations to determine the energies of electrons and optimize the structure [44,45]. The slab of the catalyst model accommodates four layers that were constructed of $4 \times 4$ unit cells of MgO (200), $1 \times 3$ unit cells of $MgCO_3$ (006), and $3 \times 3$ unit cells of $MgCO_3$ (104). The two bottom layers were constrained to prevent the displacement of an atom during the calculation and the relaxation of the two top layers was permitted to achieve surface reconfiguration. A vacuum slab with a thickness of 20 Å was projected on the top of the layer to prevent the interaction between slabs. The Brillouin zone was sampled with a $2 \times 2 \times 1$ Monkhorst-Pack grid. Spin polarization was employed for all structures to consider the ferromagnetic properties of MgO (200) and the non-magnetic properties of $MgCO_3$ (006) and $MgCO_3$ (104). The effective Hubbard U parameter ($U_{eff}$) was employed with a value of 4.0 eV for the 3d orbital of Mg in MgO (200), $MgCO_3$ (006), and $MgCO_3$ (104) [46]. Ultrasoft pseudopotentials were used to describe the core interactions with a cutoff energy of 300 eV. Convergence tolerances of $5 \times 10^{-6}$ eV atom$^{-1}$, 0.01 eV Å$^{-1}$, 0.02 GPA, and $1 \times 10^{-3}$ Å for energy, maximum force, stress, and maximum displacement were applied for the energy calculations and geometry optimizations, respectively.

The nanoclusters of $Fe_3O_4$ and $Fe_5C_2$ were built with sizes of 3.1 Å and 5.1 Å, respectively. These two nanoclusters were introduced on the top layer of the MgO (200), $MgCO_3$ (006), and $MgCO_3$ (104) slabs to simulate the interaction. Geometry optimization calculations were performed to yield the relaxed structure of the absorbates on the surface of the MgO (200), $MgCO_3$ (006), and $MgCO_3$ (104) slabs. Mulliken

population analysis was introduced by projecting plane-wave Kohn-Sham eigenstates onto the basis set of atoms. A linear combination of atomic orbitals basis sets was provided to perform the Mulliken population analysis of the resulting projected state using Mulliken formalism [47].

## 3. Results and discussion

### 3.1. Performance of Na–FeMgO$_x$-y in CO$_2$ conversion

The catalytic hydrogenation of $CO_2$ was performed over several selected catalysts at 330 °C, 3.5 MPa, and $H_2/CO_2$ ratios of 1 and 3. The reaction results collected after 80 h of the on-stream reaction are shown in Fig. 1a. Over the Na–FeMgO$_x$-5 catalyst, at a $H_2/CO_2$ ratio of 1 and gas hourly space velocity (GHSV) of 2000 mL g$^{-1}$ h$^{-1}$, the selectivity toward $C_{5+}$ was high (66.5%, hereafter excluding CO) at a $CO_2$ conversion of 19.6% with a moderate $C_2$–$C_4$ selectivity of 26.8%, whereas the selectivities toward CO (25.4%) and $CH_4$ (6.7%) were suppressed. Because of the low $CO_2$ conversion at a $H_2/CO_2$ ratio of 1, the $C_{5+}$ yield was low (9.9%, Table S1). At an increased $H_2/CO_2$ ratio of 3 and GHSV of 4000 mL g$^{-1}$ h$^{-1}$, the $CO_2$ conversion increased to 44.4% with a significant reduction of CO selectivity to 9.6% and a slight decrease in the $C_{5+}$ selectivity to 55.5%. As a result, the $C_{5+}$ yield increased up to 22.3% (Table S1). The performance of the Na–FeMgO$_x$-5 catalyst was compared with those of Na–MgO and Na–Fe$_2$O$_3$ (Fig. 1a). The use of Na–MgO resulted in a very low $CO_2$ conversion of 3.0%, indicating that the MgO site was not sufficiently active toward $CO_2$ molecules. The production of $C_{2+}$ over the Na–MgO could be due to the catalytic wall effect. The $CO_2$ conversion and $C_{5+}$ yields achieved over the Na–Fe$_2$O$_3$ catalyst (13.0% and 4.1%, respectively) were lower than those obtained over the Na–FeMgO$_x$-5 catalyst (19.6% and 9.9%, respectively, Fig. 1a). Thus, the presence of MgO$_x$ is beneficial in enhancing the $CO_2$ hydrogenation performance.

The $CO_2$ conversion and hydrocarbon selectivity were monitored by varying the reaction temperature at 3.5 MPa, 4000 mL g$^{-1}$ h$^{-1}$, and a $H_2/CO_2$ ratio of 3, and the results are shown in Fig. 1b. A high reaction temperature is beneficial for increasing the $C_{5+}$ selectivity. As the reaction temperature increased from 270 to 360 °C, the $CO_2$ conversion increased significantly from 10.2% to 49.1% and the $C_{5+}$ selectivity increased from 30.2% to 55.8%, while the selectivities toward CO and $C_2$–$C_4$ decreased drastically from 31.5% to 8.4% and from 48.7% to 30.6%, respectively. At 360 °C, the $C_{5+}$ yield reached 25.1%, which is higher than the reported yields of most previously published metal-oxide-based catalysts (Table S1, Fig. S1a). The distributions of the products over the Na–Fe$_2$O$_3$ and Na–FeMgO$_x$-5 catalysts were analyzed, and the results are shown in Fig. 1c and d. Over the Na–Fe$_2$O$_3$ catalyst at 330 °C, 3.5 MPa, 2000 mL g$^{-1}$ h$^{-1}$, and a $H_2/CO_2$ ratio of 1, the olefinic $C_2^=$–$C_4^=$ species among the overall $C_2$–$C_4$ products. The olefin-to-paraffin (O/P) ratio of the $C_2$–$C_4$ produced over the Na–Fe$_2$O$_3$ catalyst was extremely high (20.6), and that of the $C_2$–$C_{18}$ products decreased to 4.2. In contrast, over the Na–FeMgO$_x$-5 catalyst, the O/P ratios of $C_2$–$C_4$ and $C_2$–$C_{20}$ were much lower (1.6 and 3.3, respectively) than those of Na–Fe$_2$O$_3$. At the condition that produced high-yield $C_{5+}$ (360 °C, 3.5 MPa, 4000 mL g$^{-1}$ h$^{-1}$, and a $H_2/CO_2$ ratio of 3, Fig. 1e), the O/P ratios of $C_2$–$C_4$ and $C_2$–$C_{20}$ did not change significantly (2.1 and 3.3, respectively). Thus, the presence of MgO$_x$ has a detrimental effect on the formation of olefins.

The effect of MgO in the Na–FeMgO$_x$-y catalysts on $CO_2$ conversion
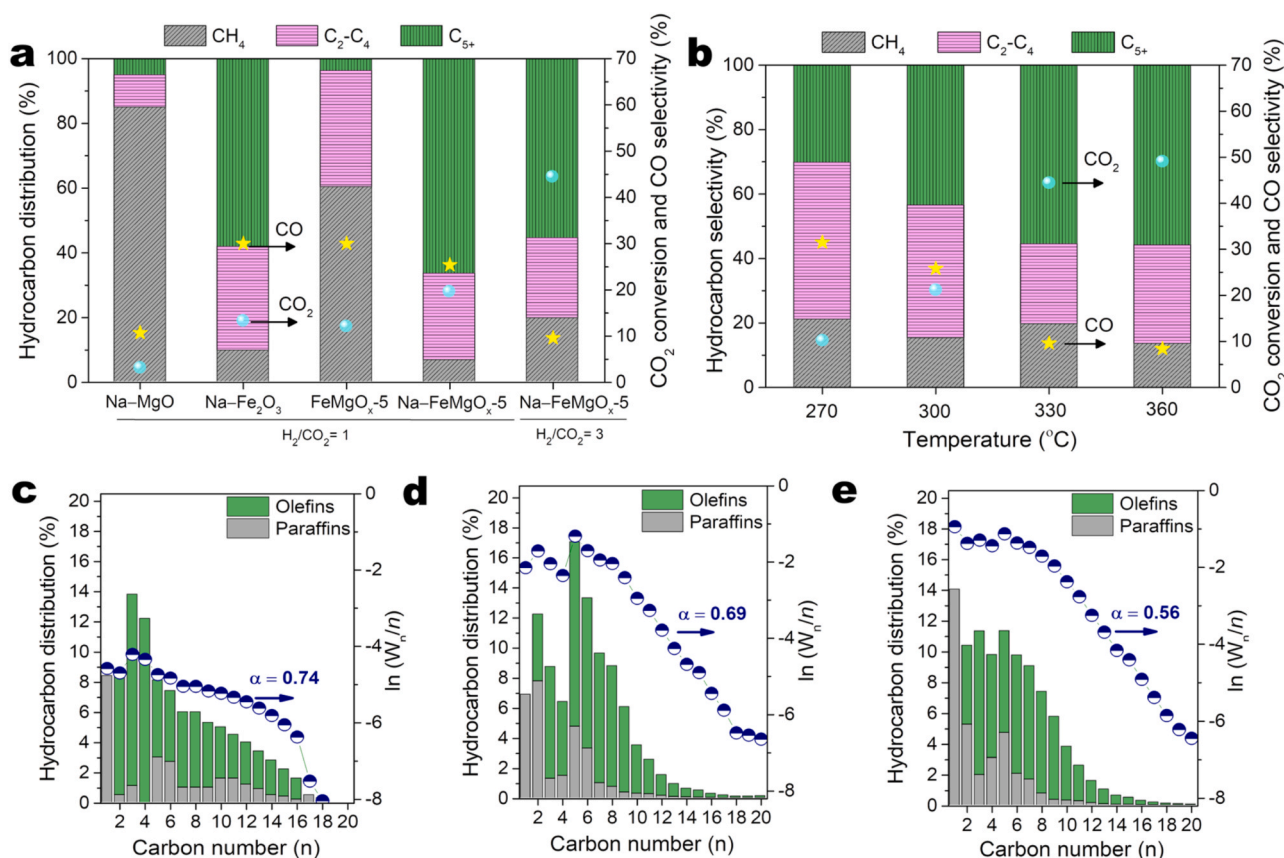
**Fig. 1.** Catalytic hydrogenation of $CO_2$ over various catalysts. (a) $CO_2$ conversion, hydrocarbon selectivity (excluding CO), and CO selectivity of various types of catalysts. The Na–FeMgO$_x$-5 catalyst was tested using two different $H_2/CO_2$ ratios of 1 and 3. (b) $CO_2$ conversion, CO selectivity, and hydrocarbon selectivity (excluding CO) of the Na–FeMgO$_x$-5 catalyst at various temperatures. Carbon-number distributions and chain growth probability (α) for the hydrocarbon species produced with the Anderson–Schulz–Flory product distribution over the (c) Na–Fe$_2$O$_3$, (d) and (e) Na–FeMgO$_x$-5 catalysts where $W_n$ is the weight fraction of the product with respect to the number ($n$) of carbon atoms. Reaction conditions of (c) and (d): 330 °C, 3.5 MPa, $H_2/CO_2$ ratio of 1, 2000 mL g$^{-1}$ h$^{-1}$ ($CO_2 = 1000$ mL g$^{-1}$ h$^{-1}$; $H_2 = 1000$ mL g$^{-1}$ h$^{-1}$), and 80 h. The formation of C$_{19+}$ was negligible. Reaction conditions of (e): 360 °C, 3.5 MPa, $H_2/CO_2$ ratio of 3, 4000 mL g$^{-1}$ h$^{-1}$ ($CO_2 = 1000$ mL g$^{-1}$ h$^{-1}$; $H_2 = 3000$ mL g$^{-1}$ h$^{-1}$), and 80 h. The formation of C$_{21+}$ was negligible. The selectivity toward oxygenated species in the water phase was < 5.0%. All catalysts were reduced in the reactor at 450 °C, 3.5 MPa, and $H_2$ flow rate of 50 mL min$^{-1}$, for 10 h.

was examined by changing the Fe and Mg contents in the catalysts (Fig. S2). As $y$ increased from 1 to 5, the $CO_2$ conversion increased from 30.3% to 44.4%, C$_{5+}$ selectivity increased from 41.7% to 55.5%, while CO selectivity decreased from 22.8% to 9.6%. A further increase in $y$ to 9 resulted in decreasing $CO_2$ conversion to 26.0% and C$_{5+}$ selectivity to 15.2%, while increasing CO selectivity to 19.9%. Thus, a balanced Fe and Mg content in the Na–FeMgO$_x$-$y$ catalysts maximize the $CO_2$ conversion and C$_{5+}$ selectivity.

The catalytic stability of Na–FeMgO$_x$-5 was maintained up to 100 h-on stream at 330 °C, 3.5 MPa, 2000 mL g$^{-1}$ h$^{-1}$, and a $H_2/CO_2$ ratio of 1 (Fig. 2a); the hydrocarbon selectivity and $CO_2$ conversion were quite stable over time, but the CO selectivity increased slightly from 19.9% to 21.8% by the end of the 100 h on stream. The slight increase in CO selectivity resulted in a marginal decrease in hydrocarbon selectivity and a slight increase in the C$_2$–C$_4$ selectivity. As the time-on-stream was extended to 670 h, a drastic decrease in the hydrocarbon selectivity from 61.5% to 0.5% was observed, along with an increase in CO selectivity from 20.0% to 48.9% (Fig. 2b). Over the Na–FeMgO$_x$-5 catalyst, the O/P ratio of C$_2$–C$_4$ was 1.6 after 50 h on-stream reaction while that of C$_2$–C$_4$ decreased to 1.1 after 670 h on-stream (Fig. 2c and d). The carbon balances of the 50 h and 670 h on-stream reactions were in the range of 90–95%.

The spent Na–FeMgO$_x$-5 catalyst collected after 670 h-on stream was regenerated by burning the coke followed by re-activation. As shown in Fig. S3, the regenerated Na–FeMgO$_x$-5 catalyst exhibited slightly lower

$CO_2$ conversion and slightly higher C$_{5+}$ selectivity as compare to its fresh counterpart.

The Na-FeMgO$_x$-5 catalysts were synthesized several times and their repeatability was evaluated by analyzing samples from the various batches. The hydrocarbon selectivity and $CO_2$ conversion were measured at 330 °C, 3.5 MPa, 4000 mL g$^{-1}$ h$^{-1}$, a $H_2/CO_2$ ratio of 3, and 50 h were consistent (Fig. S4), indicating good repeatability of the synthesis method.

### 3.2. Optimization of $CO_2$ conversion over Na–FeMgO$_x$-5

The conditions for $CO_2$ conversion over the Na–FeMgO$_x$-5 catalyst were optimized by varying the GHSV, pressure, and $H_2/CO_2$ ratio. When the GHSVs were increased from 2000 to 12,000 mL g$^{-1}$ h$^{-1}$ at 330 °C, 3.5 MPa, and a $H_2/CO_2$ ratio of 3, $CO_2$ conversion decreased from 46.9% to 30.2%, the C$_{5+}$ selectivity decreased from 57.4% to 40.9%, while the CO selectivity increased from 9.0% to 18.8% and the C$_2$–C$_4$ selectivity increased from 29.1% to 42.9% (Fig. S5a). At the low GHSV of 2000 mL g$^{-1}$ h$^{-1}$, the O/P ratios of C$_2$–C$_4$ and C$_2$–C$_{20}$ were extremely low (0.1 and 0.4, respectively, Fig. S5b). The formation of olefins was favorable in the high GHSV regime (Fig. S5d); as the GHSV increased from 2000 to 8000 mL g$^{-1}$ h$^{-1}$, the O/P ratios of C$_2$–C$_4$ and C$_2$–C$_{20}$ were increased to 1.8. The increase in GHSV reduced the hydrogenation ability of the reaction intermediates adsorbed on the catalyst surface, resulting in high olefin selectivity.
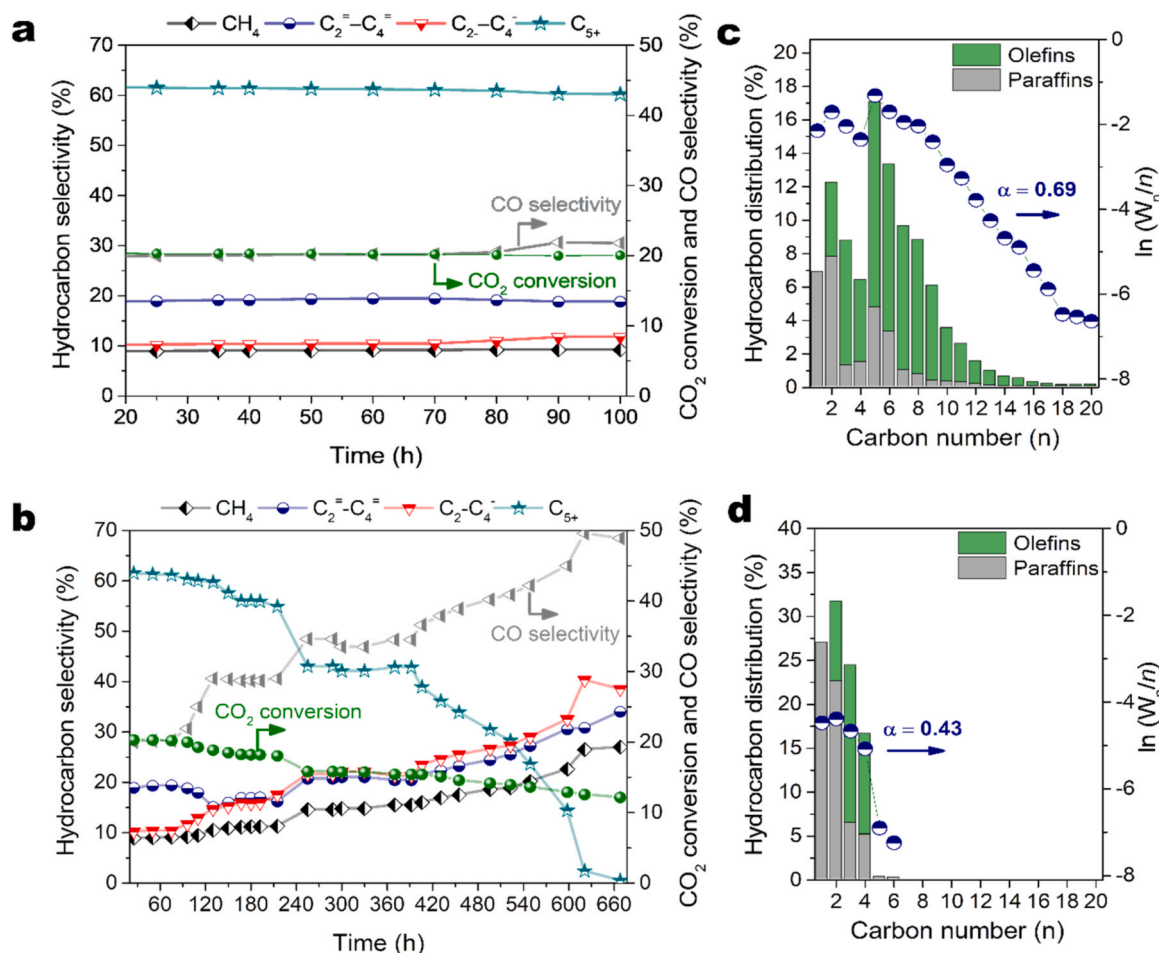
**Fig. 2.** Stability of the Na–FeMgO$_x$-5 catalyst for the reactions up to (a) 100 h and (b) 670 h on-stream. Carbon-number distributions and chain growth probability (α) for the hydrocarbon species produced with the Anderson–Schulz–Flory product distribution over the Na–FeMgO$_x$-5 catalysts (c) 80 h, and (d) 670 h, where $W_n$ is the weight fraction of the product with respect to the number ($n$) of carbon atoms. Reduction conditions: 450 °C, 3.5 MPa, and H$_2$ flow rate of 50 mL min$^{-1}$, for 10 h. Reaction conditions: 330 °C, 3.5 MPa, H$_2$/CO$_2$ ratio of 1, and 2000 mL g$^{-1}$ h$^{-1}$ (CO$_2$ = 1000 mL g$^{-1}$ h$^{-1}$; H$_2$ = 1000 mL g$^{-1}$ h$^{-1}$).

As the H$_2$/CO$_2$ ratio increased from 0.5 to 3 at 330 °C and 3.5 MPa, the CO$_2$ conversion and C$_{5+}$ yield increased significantly from 10.6% to 44.4% and from 4.6% to 22.3%, respectively, while the CO selectivity decreased from 36.8% to 9.6% respectively (Fig. S6a). The O/P ratio of C$_2$–C$_{20}$ decreased from 3.0 to 0.3 when the H$_2$/CO$_2$ ratio increased from 2 to 3, respectively, at an identical GHSV of 4000 mL g$^{-1}$ h$^{-1}$ (Fig. S6c and d), indicating that the presence of sufficient H$_2$ favors the formation of paraffins due to the excess coverage of hydrogen over the catalyst surface. The CH$_4$ selectivity increased with increasing the H$_2$/CO$_2$ ratio because of the enhanced activity for the hydrogenation of CH$_2$– monomers.

The conversion and product selectivity for CO$_2$ hydrogenation reactions was affected significantly by the reaction pressure (Fig. S7). As the pressure increased from 0.1 to 3.5 MPa at 330 °C, 4000 mL g$^{-1}$ h$^{-1}$, and a H$_2$/CO$_2$ ratio of 3, the CO$_2$ conversion and C$_{5+}$ selectivity increased significantly from 10.3% to 44.4% and from 3.3% to 55.5%, respectively, while the selectivities toward CO and C$_2$–C$_4$ decreased from 67.6% to 9.6% and from 42.2% to 24.8%, respectively. The product distribution varies significantly with changing pressure (Figs. S7b–d). As the pressure increased from 1.5 to 3.5 MPa, the O/P ratio of C$_2$–C$_{20}$ decreased from 3.3 to 0.3, indicating a strong tendency toward double-bond saturation at high pressures. Therefore, it is concluded that a high GHSV, low pressure, and low H$_2$/CO$_2$ ratio favors the formation of lower and long-chain linear α-olefins, while a low GHSV, high pressure, and high H$_2$/CO$_2$ ratio are favorable for the formation of paraffins.

### 3.3. Characterization of active sites

To investigate the potential promotional effects of MgO in the Na–FeMgO$_x$-$y$ catalysts for CO$_2$ hydrogenation and clarify the type of active sites, various characterization techniques were used to examine their microstructure and composition. The XRD patterns of calcined, reduced, and spent Na–FeMgO$_x$-5 catalysts are presented in Fig. 3. In the XRD pattern for the calcined catalyst, the peaks at 2θ = 30.1°, 35.5°, 42.9°, 57.1°, and 62.5° were assigned to the (220), (311), (400), (511), and (440) planes of Fe$_3$O$_4$ (JCPDS#79–0419), respectively, while the peaks at 36.9°, 42.9°, 62.3°, 74.6°, and 78.6° correspond to the (111), (200), (220), (311), and (222) planes of MgO (JCPDS# 45–0946), respectively. The XRD pattern of the reduced Na–FeMgO$_x$-5 catalyst exhibits intense peaks at 44.6°, 65.1°, and 85.3°, which were assigned to the (110), (200), and (211) planes of α-Fe, respectively (JCPDS# 06–0696). The weak and broad peaks at 36.3°, 42.1°, and 61.2° were attributed to the (111), (200), and (220) planes of FeO, respectively (JCPDS# 46–1312). In the typical Fe-based catalysts reported in the literature, the dominant Fe species after reduction were Fe$_3$O$_4$ and FeO [12,19,24,48]. Thus, the dominant α-Fe phase in the hydrogen-reduced Na–FeMgO$_x$-5 catalyst indicates that the presence of MgO facilitates the reduction of Fe$_3$O$_4$ to α-Fe, which may be due to the electron transfer from the basic MgO site to the Fe site [26,31,32,34,36]. The XRD patterns of the spent Na–FeMgO$_x$-5 catalyst collected after 100 h of reaction on-stream exhibited the (510), (40−2), and (31−2) planes of Hägg iron carbide (χ-Fe$_5$C$_2$) at 44.1°, 44.6°, and 44.9°, respectively (JCPDS#

**Fig. 3.** XRD patterns of calcined, reduced, and spent Na–FeMgO$_x$-5 catalysts. Calcination conditions: 600 °C and static air for 6 h. Reduction conditions: 450 °C, 3.5 MPa, and H$_2$ flow rate of 50 mL min$^{-1}$, for 10 h. Reaction conditions: 330 °C, 3.5 MPa, H$_2$/CO$_2$ ratio of 1, 2000 mL g$^{-1}$ h$^{-1}$ (CO$_2$ = 1000 mL g$^{-1}$ h$^{-1}$; H$_2$ = 1000 mL g$^{-1}$ h$^{-1}$) for 100 h.

36–1248), and the peaks associated with Fe$_3$O$_4$. Thus, during the reaction, the α-Fe phase was transformed into Fe$_3$O$_4$ and χ-Fe$_5$C$_2$, which have been proposed as the active sites for RWGS and FTS reactions, respectively [16,48]. In addition, MgO was transformed into MgCO$_3$ during CO$_2$ conversion, as confirmed by the appearance of new peaks at 32.6°, 35.8°, and 46.7° in the XRD pattern of spent catalyst, which correspond to the (104), (006), and (202) planes of MgCO$_3$, respectively (JCPDS# 78–2442). The strong tendency for MgO to adsorb CO$_2$ under the given reaction conditions resulted in the conversion of MgO to MgCO$_3$ [49]. Thus, during CO$_2$ hydrogenation, the promotional effect associated with Mg species in the Na–FeMgO$_x$-$y$ catalyst should be based on the MgCO$_3$ compound, rather than MgO, metallic Mg$^0$, or partially oxidized MgO$_x$ (x < 1).

To examine the effect of MgCO$_3$ on the phase and morphology changes of the catalyst during CO$_2$ hydrogenation, XRD patterns and TEM images of the calcined, reduced, and spent Na–FeMgO$_x$-$y$ catalysts with varying Fe and Mg contents were obtained. As shown in Fig. S8, in the XRD patterns of Fe-poor Na–FeMgO$_x$-$y$ catalysts ($y \leq 2$), peaks related to highly crystalline MgO at 42.9°, 62.3°, 74.6°, and 78.6° were observed, while in the pattern of medium-to-high Fe-containing Na–FeMgO$_x$-$y$ catalysts ($5 \leq y \leq 9$), the evolution of the Fe$_3$O$_4$ phase with a progressive decrease in the intensity of the peaks associated with MgO was observed. In addition, with increasing Fe content in the Na–FeMgO$_x$-$y$ catalysts, the MgO peaks at 42.9° and 62.3° were progressively upshifted to 43.1° and 62.5°, respectively. Because the atomic radius of Fe$^{2+}$ is smaller (75 pm) than that of Mg$^{2+}$ (86 pm), the

incorporation of Fe$^{2+}$ into the MgO domain decreases the lattice spacing. In the Fe-rich Na–FeMgO$_x$-$y$ catalysts ($y \geq 7$), a small peak at 33.2° was observed, which was attributed to the (104) plane of the α-Fe$_2$O$_3$ phase. Thus, the presence of sufficient MgO suppresses the formation of the fully oxidized hematite phase during calcination under static air. The crystallite size of Fe$_3$O$_4$ in the calcined catalysts, measured from the width of the (311) peak and the Scherrer equation, decreased in the order of Na–FeMgO$_x$-7 (11.4 nm) > Na–FeMgO$_x$-9 (11.0 nm) > Na–Fe$_3$O$_4$ (10.5 nm) > Na–FeMgO$_x$-5 (6.9 nm) > Na–FeMgO$_x$-2 (1.2 nm) (Table S3); the presence of a balanced amount of MgO in the Na–FeMgO$_x$-5 catalyst limited the growth of Fe$_3$O$_4$ crystal. The morphological and phase characteristics of the calcined Na–FeMgO$_x$-5 catalyst were further analyzed by HR–TEM and HAADF–STEM with EDS mapping. The calcined Na–FeMgO$_x$-5 catalyst exhibited nanosized particles with diameters in the range of 20–30 nm (Figs. S9a–c). The HR–TEM image reveals the presence of Fe$_3$O$_4$ phase with lattice spacings of 2.53 Å (311) and 2.96 Å (220), while the crystalline MgO phase was not observed (Figs. S9d and e). In the HAADF–STEM image and corresponding EDS mapping of the calcined Na–FeMgO$_x$-5 catalyst (Figs. S9f–k), the Fe and Mg species were uniformly distributed, but Fe- and Mg-rich nanodomains with sizes of 20–30 nm were observed.

The XRD patterns of the reduced Na–FeMgO$_x$-$y$ catalysts with $1 \leq y \leq 5$ (Fig. S10) show that the dominant species were MgO and α-Fe with a small fraction of FeO. In the Fe-rich Na–FeMgO$_x$-$y$ catalysts ($y \geq 7$), a crystalline MgO phase was not observed, while α-Fe and FeO were the dominant crystalline species. Notably, the absence of the Fe$_3$O$_4$ phase in all reduced catalysts demonstrated the strong reduction tendency of the Fe$_3$O$_4$ phase to be reduced to α-Fe and FeO phases in the presence of MgO. The crystallite size of α-Fe, measured using the width of the (110) peak and the Scherrer equation, decreased in the order of Na–FeMgO$_x$-5 (89.9 nm) > Na–FeMgO$_x$-9 (42.3 nm) > Na–FeMgO$_x$-2 (37.5 nm) > Na–FeMgO$_x$-7 (36.4 nm) > Na–Fe$_3$O$_4$ (16.7 nm) (Table S4). The preferential growth of the α-Fe phase at $y = 5$ may be due to the sufficient amount of MgO acting as an electron donor as well as sufficient amount of Fe species available in the bimetallic catalyst. As shown in Fig. S11a–e, the reduced Na–FeMgO$_x$-5 catalyst exhibited well-faceted crystalline particles of α-Fe phase, which agrees well with the XRD results. The particle size increased from 20 to 30 nm (calcined) to 50–100 nm (reduced). The well-faceted particles consisted of a mixed phase containing both Fe and Mg species in close proximity, while the irregular particles are considered isolated MgO domains (Fig. S11f–k).

In the XRD pattern of the spent Na–FeMgO$_x$-$y$ catalysts that were collected after 50 h of the on-stream reaction (Fig. S12), the α-Fe phase was transformed into Fe$_3$O$_4$ and χ-Fe$_5$C$_2$ phases, and the MgO phase was converted to MgCO$_3$. The formation of χ-Fe$_5$C$_2$ was activated in the Fe-rich Na–FeMgO$_x$-$y$ catalysts ($y \geq 5$). To understand the deactivation behaviors of the Na–FeMgO$_x$-5 catalysts, XRD patterns of the spent catalysts after various times-on-stream (80–670 h) were collected (Fig. 4). The spent catalyst collected after 80 h of on-stream reaction was rich in χ-Fe$_5$C$_2$ and MgCO$_3$ phases. As the reaction time increased to 100 h, the intensity of the peaks associated with χ-Fe$_5$C$_2$ decreased, and a further increase in the reaction time to 670 h resulted in almost complete disappearance of the χ-Fe$_5$C$_2$ phase. As the reaction time increased from 80–670 h, the intensity of the peaks associated with Fe$_3$O$_4$ and MgCO$_3$ did not change significantly. Crystalline Fe$_3$O$_4$ remained in the spent catalysts sampled at reaction times of 80–670 h. A slight increase in the crystal size of MgCO$_3$ from 31.5 to 38.2 nm was observed when the reaction time increased from 80 h to 670 h, respectively (Table S5). In addition, the Fe$_2$O$_3$ phase did not form during the 670 h of on-stream reaction. Thus, the rapid decrease in the C$_{5+}$ selectivity after 400 h on-stream (Fig. 2b) was attributed to the transformation of the χ-Fe$_5$C$_2$ phase to Fe-oxide phases. The spent Na–FeMgO$_x$-5 catalyst collected after 100 h of on-stream reaction, which was still active towards FTS (Fig. 2a), exhibited large elliptical shape MgCO$_3$ domains with surfaces decorated with small irregular Fe$_3$O$_4$ and χ-Fe$_5$C$_2$ particles with sizes of 50–100 nm (Fig. S13). In
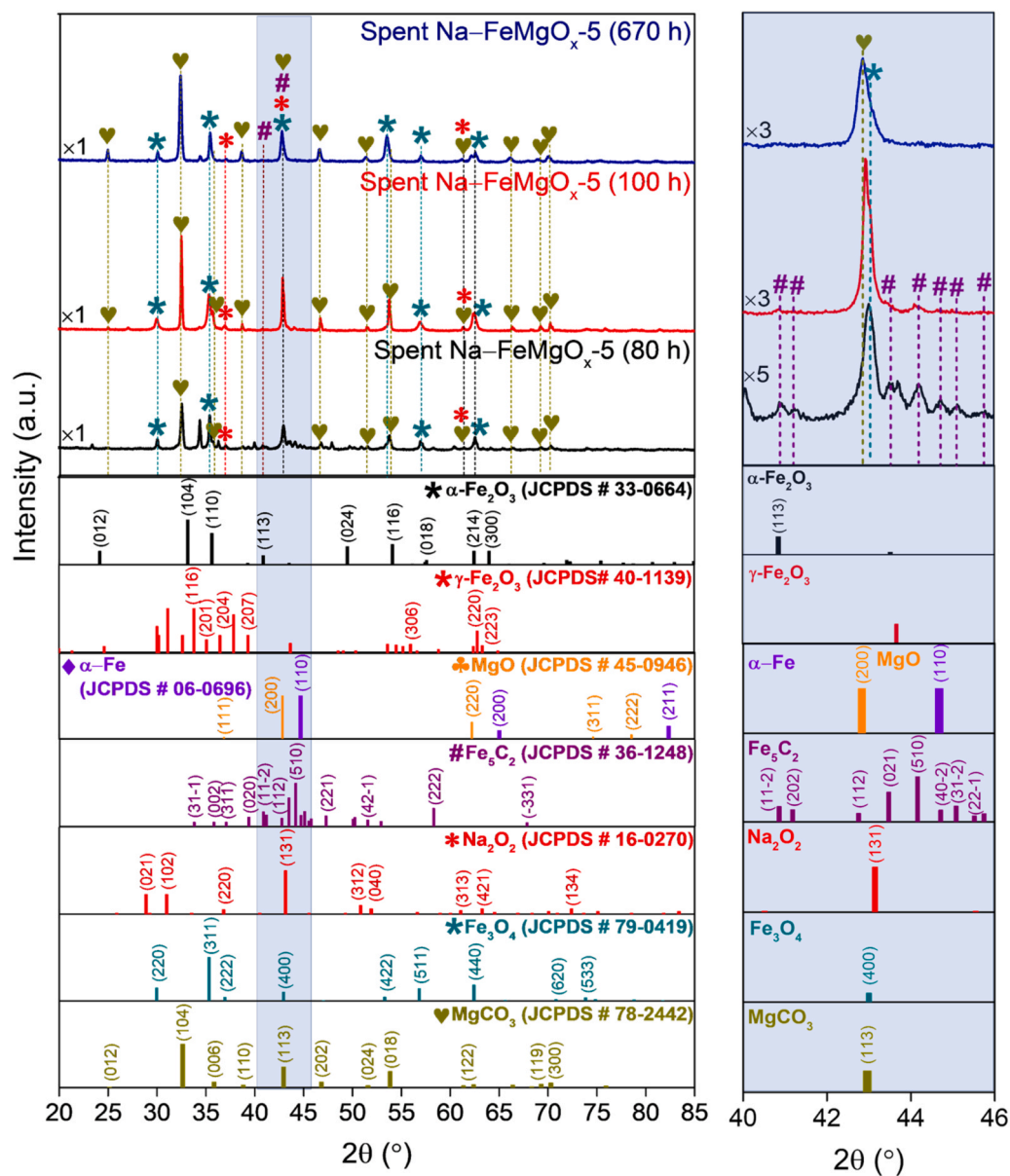
**Fig. 4.** XRD patterns of spent Na–FeMgO$_x$-5 catalysts collected after reaction times of 80, 100, and 670 h. Reduction conditions: 450 °C, 3.5 MPa H$_2$ pressure, and 50 mL min$^{-1}$ for 10 h. Reaction conditions: 330 °C, 3.5 MPa, H$_2$/CO$_2$ ratio of 1, and 2000 mL g$^{-1}$ h$^{-1}$ (CO$_2$ = 1000 mL g$^{-1}$ h$^{-1}$; H$_2$ = 1000 mL g$^{-1}$ h$^{-1}$).



**Fig. 5.** (a–d) EDS images of the calcined, reduced, and spent Na–FeMgO$_x$-5 catalysts. Reduction conditions: 450 °C, 3.5 MPa H$_2$ pressure, and 50 mL min$^{-1}$ for 10 h. Reaction conditions: 330 °C, 3.5 MPa, H$_2$/CO$_2$ ratio of 1, and 2000 mL g$^{-1}$ h$^{-1}$ (CO$_2$ = 1000 mL g$^{-1}$ h$^{-1}$; H$_2$ = 1000 mL g$^{-1}$ h$^{-1}$) for 100 and 670 h.

contrast, the spent Na–Fe$_3$O$_4$ catalyst collected after 100 h of on-stream reaction exhibited highly aggregated micron-sized particles (Fig. S14). Thus, the spatial distribution of active Fe nanodomains over the surface of MgCO$_3$ particles make the catalyst highly active for the synthesis of C$_{5+}$ via RWGS and FTS reactions. This indicates that the MgCO$_3$ domains act as a structural promotor in early stage of the reaction. The spent Na–FeMgO$_x$-5 catalyst collected after 670 h on-stream, which was not active toward the FTS reaction (Fig. 2b), showed that most of the isolated χ-Fe$_5$C$_2$ particles were decomposed to Fe oxides, which "wetted" the surface of the MgCO$_3$ particles (Fig. S15). Irregularly shaped Fe$_3$O$_4$-rich particles were randomly distributed on the surface of the spherical mixed Fe-oxide and MgO particles; this microstructure is thought to be the reason for the active RWGS reaction after 670 h (Fig. 2b). In summary, as shown in Fig. 5, the α-Fe and MgO mixed phases in the reduced Na–FeMgO$_x$-5 catalyst were separated into discrete Fe$_3$O$_4$/χ-Fe$_5$C$_2$ and MgCO$_3$ domains during the active CO$_2$ hydrogenation to C$_{5+}$. The deactivation of the Na–FeMgO$_x$-5 catalyst was caused by the reoxidation of the χ-Fe$_5$C$_2$ phase to highly pulverized Fe oxides, and subsequent "wetting" of the pulverized Fe oxides on the surface of MgCO$_3$. The O$_2$-TPO was performed to confirm the oxidation of χ-Fe$_5$C$_2$ phase and coke in the spent catalysts (Fig. S16). The spent Na–FeMgO$_x$-5 catalyst collected after 100 h-on stream exhibited broad peaks at 150–420 °C, which can be assigned to the decomposition of Fe carbide species, and an intense peak centered at 453 °C, which corresponds to the oxidative decomposition of graphitic or surface polymerized carbon [50,51]. Contrarily, the spent Na–FeMgO$_x$-5 catalyst collected after 670 h-on stream only exhibited high temperature peaks centered at 468 and 489 °C, indicating only the high-molecular-weight carbons were deposited on the catalyst surface. Therefore, the absence of Fe carbide species in the spent catalyst collected after 670 h-on stream confirms the loss of C–C coupling sites.

The chemical compositions and oxidation states of the fresh, reduced, and spent Na–Fe$_3$O$_4$ and Na–FeMgO$_x$-5 catalysts were analyzed using XPS. The C 1 s spectra of the fresh and reduced Na–Fe$_3$O$_4$ catalysts were deconvoluted into peaks corresponding to C–C at 284.8 eV, C–O–C at 286.9 eV, and C=O at 288.8 eV due to the contamination with organic species when exposed to air, while the spent Na–Fe$_3$O$_4$ catalyst exhibited an additional Fe–C peak at 283.2 eV [52] (Fig. S17a). The presence of the peak associated with carbonate (CO$_3^{2-}$) at 290.1 eV [53]

in the spectra of the calcined and spent Na–FeMgO$_x$-5 catalysts, which was not observed for the Na–Fe$_3$O$_4$ counterparts, was attributed to the use of Na$_2$CO$_3$ as the precipitating agent in the catalyst synthesis process (Fig. S17b). The intensity of the carbonate peak was higher in the spectrum of the spent Na–FeMgO$_x$-5 catalyst collected after 670 h of on-stream reaction due to the transformation of MgO to MgCO$_3$ during CO$_2$ hydrogenation. The intensity of the Fe–C peak in the spectrum of the spent Na–FeMgO$_x$-5 catalyst collected after 100 h of on-stream reaction was much higher than that of the spent Na–Fe$_3$O$_4$ catalyst; this indicates that the presence of MgO contributes to the formation of iron carbide phases at the initial stage of the reaction. The O 1 s spectra of the Na–Fe$_3$O$_4$ and Na–FeMgO$_x$-5 catalysts were deconvoluted into the peaks corresponding to lattice oxygen at 530.1 eV, oxygen vacancies (O$_v$) at 531.1 eV, C=O at 532.2 eV, CO$_3^{2-}$ at 532.6 eV, and C–O/H$_2$O at 533.6 eV (Figs. S17c, d) [54]. The O$_v$ is considered to be active for the adsorption of CO$_2$ during CO$_2$ hydrogenation [12,55]. Based on the Fe loading in the Na–Fe$_3$O$_4$ and Na–FeMgO$_x$-5 catalysts (Table S6) and assuming the negligible formation of O$_v$ in the MgO domain, the amount of O$_v$ per mole of Fe in the reduced Na–FeMgO$_x$-5 catalyst was larger than that in the reduced Na–Fe$_3$O$_4$. Thus, the ability of MgO to donate its electrons to Fe species could facilitate the formation of O$_v$ in the Fe oxides in the reduced and spent catalysts collected after 100 h-on stream. The reduction of O$_v$ in the spent catalyst (670 h) may be due to its surface oxidation during CO$_2$ hydrogenation. In the Fe 2p$_{3/2}$ high-resolution XPS spectrum of the fresh Na–Fe$_3$O$_4$ catalyst (Fig. 6a), three peaks were observed at 709.7, 711.4 and 713.3 eV, which correspond to octahedral-coordinated Fe$^{2+(oh)}$, octahedral-coordinated Fe$^{3+(oh)}$ and tetrahedral-coordinated Fe$^{3+(th)}$, respectively [56,57]. The Fe 2p$_{3/2}$ spectra of the reduced Na–Fe$_3$O$_4$ catalyst was deconvoluted into peaks related to Fe$^0$ at 706.4 eV, FeO at 708.5 eV, Fe$^{2+(oh)}$ at 709.7 eV, Fe$^{3+(oh)}$ at 711.4 eV, and Fe$^{3+(th)}$ at 713.3 eV, while the presence of Fe–C at 707.5 eV was observed in the spent Na–Fe$_3$O$_4$ catalyst [56,57]. The intensity of the Fe$^0$ peak in the spectrum of the reduced Na–FeMgO$_x$-5 catalyst was much higher than that of the reduced Na–Fe$_3$O$_4$ catalyst (Fig. 6b). Again, the presence of MgO facilitated the formation of Fe$^0$, probably because of electron transfer from MgO to the Fe phase. The spent Na–FeMgO$_x$-5 catalyst collected after 670 h of the on-stream reaction did not exhibit Fe–C bond, which agrees well with the XRD results. As the time-on-stream increased to 670 h, the formation of MgCO$_3$
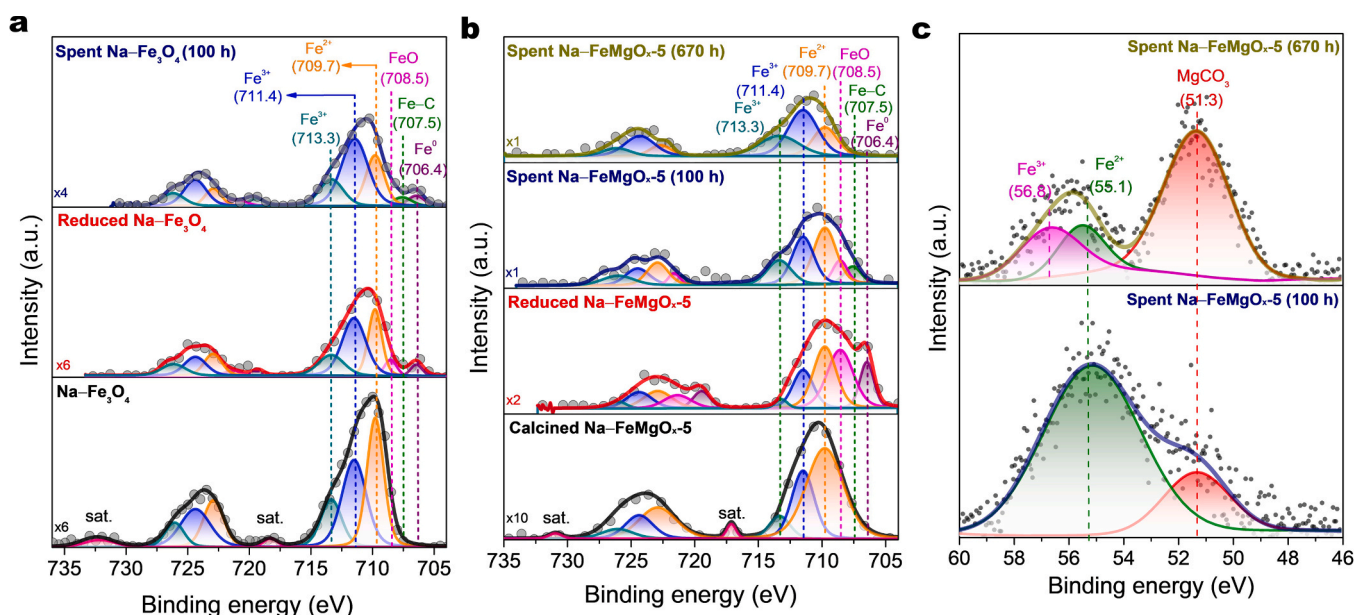


**Fig. 6.** XPS profiles of the calcined, reduced, and spent Na–Fe$_3$O$_4$ and Na–FeMgO$_x$-5 catalysts in the (a-b) Fe 2p region, and (c) Mg 2p and Fe 3p region. Reduction conditions: 450 °C, 3.5 MPa H$_2$ pressure, and 50 mL min$^{-1}$ for 10 h. Reaction conditions: 330 °C, 3.5 MPa, H$_2$/CO$_2$ ratio of 1, and 2000 mL g$^{-1}$ h$^{-1}$ (CO$_2$ = 1000 mL g$^{-1}$ h$^{-1}$; H$_2$ = 1000 mL g$^{-1}$ h$^{-1}$).
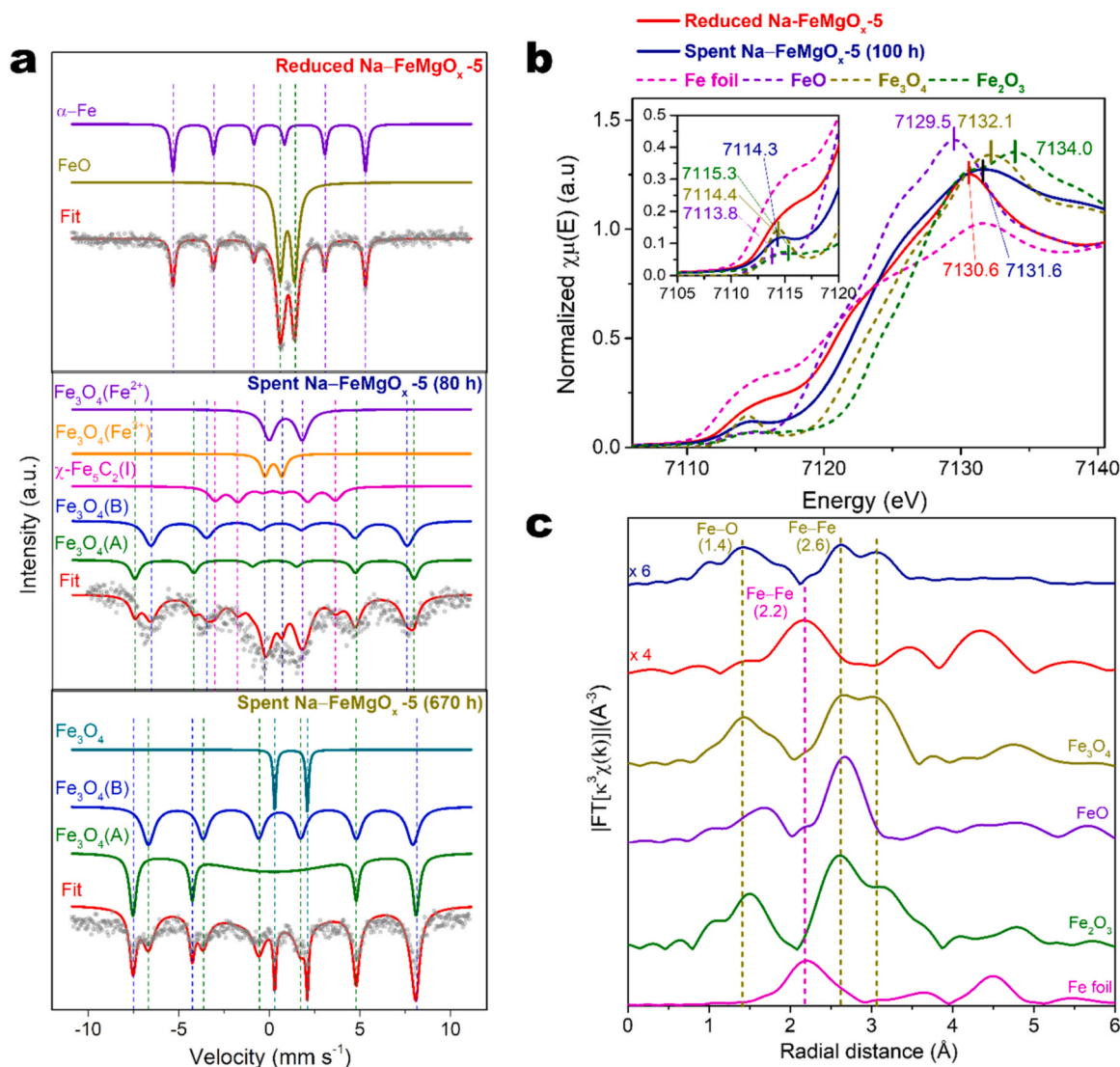
**Fig. 7.** (a) Mössbauer spectra, (b) normalized Fe K-edge XANES spectra, and (c) $k^3$-weighted Fourier transforms (FTs) of the normalized Fe K-edge EXAFS spectra ($\kappa^3\chi(k)$) of the reduced and spent Na–FeMgO$_x$-5 catalysts. Reduction conditions: 450 °C, 3.5 MPa H$_2$ pressure, and 50 mL min$^{-1}$ for 10 h. Reaction conditions: 330 °C, 3.5 MPa, H$_2$/CO$_2$ ratio of 1, and 2000 mL g$^{-1}$ h$^{-1}$ (CO$_2$ = 1000 mL g$^{-1}$ h$^{-1}$; H$_2$ = 1000 mL g$^{-1}$ h$^{-1}$).

was facilitated by the peak at 51.3 eV [58] in the XPS spectrum of the spent Na–FeMgO$_x$-5 catalyst (Fig. 6c).

To verify the active sites of iron in the Na–FeMgO$_x$-5 catalyst, the reduced and spent catalysts were analyzed by Mössbauer spectroscopy (Fig. 7a, Table S7). The reduced catalyst consisted of two discernible phases of α-Fe (38.4%) and FeO (61.6%). The spent catalyst collected after 80 h of the on-stream reaction exhibited the coexistence of RWGS-active Fe$_3$O$_4$ (79.6%) and FTS-active χ-Fe$_5$C$_2$ (20.4%) phases. Thus, some fraction of α-Fe and FeO phases in the reduced catalyst were converted to χ-Fe$_5$C$_2$, while the remaining fraction was converted to Fe$_3$O$_4$ during CO$_2$ hydrogenation. The spent Na–FeMgO$_x$-5 catalyst collected after 80 h on-stream exhibited sextets with the hyperfine fields of 480.9 and 440.7 kOe, which correspond to the Fe$_3$O$_4$-A (containing tetrahedral Fe$^{3+}$ ions) and Fe$_3$O$_4$-B (containing octahedral Fe$^{2+}$ and Fe$^{3+}$ ions) phases, respectively, and that at 207.0 kOe which corresponds to the Fe$_5$C$_2$ (I) phase. Contrarily, the Fe$_3$O$_4$-A, Fe$_3$O$_4$-B, and Fe$_3$O$_4$ phases were dominant species in the spent catalyst collected after 670 h on-stream. Thus, the progressive oxidation of χ-Fe$_5$C$_2$ to Fe$_3$O$_4$ was the main deactivation mechanism of the C–C coupling reaction, and thus CO selectivity was increased up to 50% after 670 h of reaction (Fig. 2b).

The local chemical states of absorbing centers of the reduced and spent Na–FeMgO$_x$-5 catalysts were measured by XAS. In the Fe K-edge XANES spectra (Fig. 7b), the pre-edge energies of the reduced Na–FeMgO$_x$-5 catalyst, which correspond to the 1 s → 3d electron transition, approached those of the Fe$^0$ foil reference. The presence of the white-line peak at 7130.6 eV, which is between the peaks of the FeO and Fe$_3$O$_4$ reference powders, indicates that some of the iron phases in the reduced Na–FeMgO$_x$-5 catalyst exhibited oxidation states between + 2 and + 3. The white-line peak of the spent catalyst collected after 100 h of reaction upshifted slightly to 7131.6 eV compared to that of the reduced catalyst, indicating that oxidation occurred during CO$_2$ conversion. In the Fourier transform (FT) $k^3$-weighted EXAFS spectra, the major scattering path of the reduced Na–FeMgO$_x$-5 catalyst appeared at 2.2 Å, which was assigned to metallic Fe–Fe coordination. The peak at 1.4 Å in the spent Na–FeMgO$_x$-5 catalyst corresponds to the first shell Fe–O scattering path of Fe$_3$O$_4$, and the peak at 2.6 Å corresponds to the second shell Fe–Fe scattering path of iron-oxide phases.

The reduction behaviors of the calcined catalysts were observed using H$_2$–TPR (Fig. 8a). The H$_2$ consumption of the Na–MgO sample was negligibly small because MgO is hardly reduced below 1000 °C [59]. The spectrum of Na–Fe$_3$O$_4$ shows two major peaks at 367 and 685 °C,
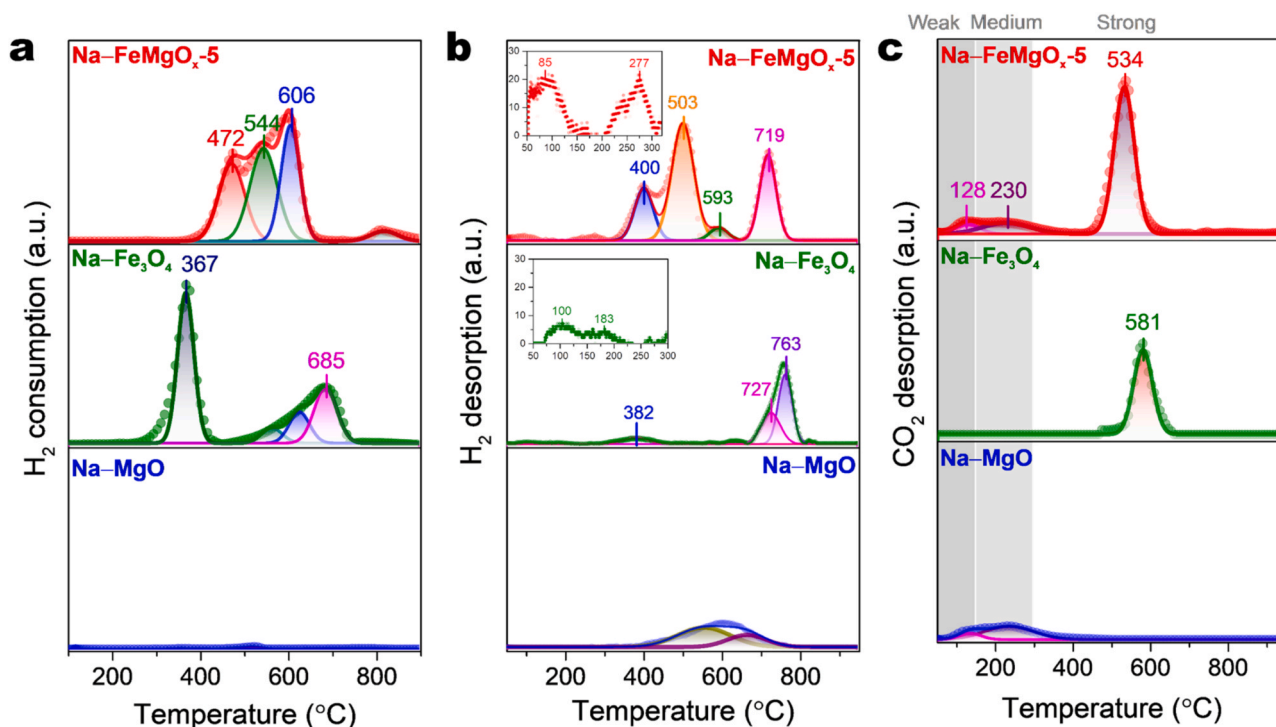
**Fig. 8.** (a) $H_2$–TPR, (b) $H_2$–TPD, and (c) $CO_2$–TPD profiles of the catalysts. Calcination conditions: 600 ℃ under static air for 6 h, Reduction conditions: 450 ℃, 3.5 MPa $H_2$ pressure, and 50 mL min$^{-1}$ for 10 h.

which correspond to the stepwise reduction of $Fe^{3+} \rightarrow Fe_3O_4 \rightarrow Fe^0$ [60]. The incorporation of MgO into Na–$Fe_3O_4$ decreased the reduction temperature of $Fe_3O_4 \rightarrow Fe^0$ because of the electron transfer from MgO to $Fe_3O_4$ and nanosized Fe-oxide domains dispersed on the MgO surface (Fig. 8). The total $H_2$ consumption of the Na–$Fe_3O_4$ catalyst was 2.943 mmol g$^{-1}$, which is similar to the theoretical $H_2$ consumption that is required to completely reduce $Fe_3O_4$ to $Fe^0$ (2.741 mmol g$^{-1}$, Table S8). The smaller $H_2$ consumption over the Na–FeMgO$_x$-5 catalyst (1.803 mmol g$^{-1}$) was caused by the presence of barely reducible MgO.

The dissociative adsorption and spillover effect of hydrogen on the catalyst surface were examined by $H_2$–TPD (Fig. 8b). The desorbed species were monitored using the QMS residual gas analyzer during TPD analysis, and the profiles for $H_2$ desorption were corrected using the mass profile of $m/z = 2$ (Fig. S18). The spectrum of the Na–$Fe_3O_4$ catalyst exhibited a weak and broad low-temperature peak below 300 °C; the broad peak centered at 100 °C was assigned to the weakly adsorbed $H_2$ on the terrace site and that at 183 °C could correspond to $H_2$ adsorption on the defect or hollow sites [60,61]. The peaks above 300 °C may be attributed to $H_2$ desorption from the –OH group of non-reduced Fe oxides [62]. More $H_2$ was desorbed from the Na–FeMgO$_x$-5 catalyst than the Na–$Fe_3O_4$ catalyst at temperatures below 300 °C. The Fe loading in the Na–FeMgO$_x$-5 catalyst was approximately half of that in the Na–$Fe_3O_4$ catalyst, and electron transfer from the MgO to the Fe site can suppress $H_2$ adsorption [36] (which may be a result of increased Pauli repulsion between the electrons at the surface and the approaching $H_2$ [63]). Considering these factors, the reduction in the Fe domain size is thought to be the dominant mechanism for enhancing $H_2$ adsorption on the Na–FeMgO$_x$-5 catalyst; in other words, the potential suppression of $H_2$ adsorption by electron transfer was overcome by the increased number of adsorption sites by the structural promotional effect of MgO (Fig. S11).

The basicity and basic strength of the catalysts were examined using $CO_2$–TPD (Fig. 8c). Again, the desorbed species were monitored using the QMS residual gas analyzer, and the profiles for $CO_2$ desorption were corrected using the mass profile of $m/z = 44$ (Fig. S19). The desorption peaks were classified into weak (< 150 ℃), moderate (151–300 ℃), and

strong (> 301 ℃) basic sites, which arise from the formation of bi-carbonates on the weak basic Brønsted –OH groups, bidentate carbonates on metal–oxygen pairs, and unidentate carbonates on the low-coordinated surface $O^{2-}$ anions, respectively [64,65]. The spectrum of the Na–MgO sample exhibited weak and broad peaks at temperatures below 400 ℃, while the Na–$Fe_3O_4$ catalyst shows a relatively intense peak at 581 ℃. After the incorporation of MgO into Na–$Fe_3O_4$, a peak associated with $CO_2$ desorption from the MgO surface was observed, and the intensity of the peak that corresponds to $CO_2$ desorption from the strong basic (Fe)–$O^{2-}$ sites at 530 ℃ increased significantly. The total amount of $CO_2$ desorbed from the Na–FeMgO$_x$-5 catalyst surface was approximately nine times larger than that desorbed from the Na–$Fe_3O_4$ catalyst surface (Table S9). Thus, the presence of MgO decreased the Fe-oxide domain size and facilitated the formation of low-coordinated oxygen anions via electron donation, which enhances $CO_2$ adsorption on strong basic sites. Considering that the typical temperature for $CO_2$ hydrogenation over the Fe-based catalyst is above 300 ℃, enhanced $CO_2$ adsorption on strong basic sites is the dominant factor enhancing $CO_2$ hydrogenation, while $CO_2$ adsorption on the MgO site contributes only slightly to $CO_2$ hydrogenation.

The textural properties of the calcined, reduced, and spent Na–FeMgO$_x$-$y$ catalysts were examined by analyzing their $N_2$ adsorption–desorption isotherms. The BET surface area of the calcined Na–FeMgO$_x$-5 catalyst (31.7 m$^2$ g$^{-1}$) was smaller than those of the other Na–FeMgO$_x$-$y$ catalysts with different Fe loadings (Table S3). After reduction, the preferential formation of α-Fe and interparticle agglomeration decreased the BET surface area of Na–FeMgO$_x$-5 to 9.5 m$^2$ g$^{-1}$ (Table S4). As the time-on-stream increased from 50 to 670 h, the surface area of the spent catalysts progressively decreased from 8.6 to 3.8 m$^2$ g$^{-1}$, indicating that the exposure of the catalyst to the high reaction temperature results in some aggregation of the catalyst particles (Table S5).

### 3.4. Promotional effect and deactivation mechanism

To investigate the promotional effect of MgO and $MgCO_3$ during $CO_2$

hydrogenation, DFT simulations were performed to explain the inter-action between magnesium interfaces and iron-oxide nanoclusters. The structures of the MgO (200), $MgCO_3$ (006), and $MgCO_3$ (104) slabs are shown in Fig. S20. The $MgCO_3$ (104) facet was the most abundant structure (Fig. 4), while the $MgCO_3$ (006) facet was chosen for comparison. The adsorption geometries of $Fe_5C_2$ and $Fe_3O_4$ nanoclusters on the MgO (200), $MgCO_3$ (006), and $MgCO_3$ (104) slabs are shown in Figs. S21 and S22, respectively. Based on Mulliken population analysis, the number of electrons transferred from MgO (200) to $Fe_5C_2$ was high (–0.789 $q_e$, Fig. S21a). Fewer electrons were transferred from the $MgCO_3$ (104) slab to $Fe_5C_2$ (–0.254 $q_e$), while electron transfer did not occur from $MgCO_3$ (006) to $Fe_5C_2$ (Fig. S21b and c, respectively). The amounts of electrons transferred from MgO (200), $MgCO_3$ (104), and $MgCO_3$ (006) to $Fe_3O_4$ were similar to those transferred to $Fe_5C_2$ (Fig. S22). Thus, the electron donation ability of MgO was much higher than that of $MgCO_3$. The partial density of states (PDOS) of $Fe_5C_2$ and $Fe_3O_4$, which were calculated based on the adsorption of nanoclusters, indicate the downshifting of D-band centers consistent with electron transfer from the Mg to Fe species (Fig. S23). The presence of oxygen vacancy sites on the $MgCO_3$ (104) surface may increase its surface energy, which can contribute the stronger interactions with Fe species compared to the $MgCO_3$ (006) surface.

Based on the catalyst characterization and DFT simulation results, it is concluded that MgO acts as an electronic promoter during the catalyst reduction and initial stages of $CO_2$ hydrogenation (up to 120 h-on stream). The almost complete reduction of $Fe_3O_4$ to α-Fe during the reaction demonstrates the tendency of MgO to transfer its electrons to Fe-oxide phases (Fig. 3). In addition, the possibility of electron transfer from MgO to $Fe_3O_4$ and χ-$Fe_5C_2$ at the early stage of reaction should not be excluded, which could contribute to enhancing the C–C coupling reaction by facilitating the strong chemisorption of $CO_2$. Thus, the presence of MgO as an electronic promoter can increase the $C_{5+}$ yield at the early stage of the reaction (Fig. 2, Table S1), which agrees well with previous reports [28,33,34,36,38]. In addition, the presence of MgO facilitates the adsorption of $H_2$ on Fe sites by limiting the Fe domain size (Fig. 8b). Furthermore, the increased number of $O_v$ formed in the presence of MgO can facilitate $CO_2$ adsorption (Figs. S17c and d). Thus, MgO acts as both an electronic and structural promoter in the Na–FeMgO$_x$-5 catalyst. Despite the promising roles of MgO as a promoter, MgO is not stable during $CO_2$ hydrogenation and is progressively converted to $MgCO_3$ (Fig. 4). The DFT simulation results indicated that fewer electrons are transferred from $MgCO_3$ (104) to $Fe_3O_4$ and χ-$Fe_5C_2$ than from MgO (200), while the $MgCO_3$ (006) facet did not transfer its electrons to the Fe species. The decomposition of $MgCO_3$ to MgO during the coke burning of the spent Na–FeMgO$_x$-5 collected after 670 h-on stream at 450 °C and subsequent reactivation under the $H_2$ flow mostly restored the $CO_2$ conversion performance of the fresh catalyst (Fig. S3). Therefore, the progressive transformation of MgO to $MgCO_3$ during $CO_2$ hydrogenation suppresses the strong electronic promotional effects associated with MgO, leading to the reoxidation of χ-$Fe_5C_2$ to Fe oxide phases (Fig. 5) and the decrease in $CO_2$ conversion and $C_{5+}$ selectivity (Fig. 2**b**).

## 4. Conclusion

In summary, we demonstrated that the bifunctional Na–FeMgO$_x$-5 catalyst can produce a high $C_{5+}$ yield of 25.1% with a $CO_2$ conversion of 49.1% at a $H_2/CO_2$ ratio of 3, at the early stage of reaction. Owing to the electronic promotion behavior of MgO, the incorporation of MgO into the Fe-based catalyst increases the reducibility of iron oxides to metallic α-Fe. The bimetallic Na–FeMgO$_x$-5 catalyst facilitates the formation of the RWGS-active $Fe_3O_4$ phase and FTS-active χ-$Fe_5C_2$ phase from α-Fe during the early stage of reaction (120 h on-stream). In addition, the MgO promoter enhances the adsorption of $CO_2$ and $H_2$ and subsequently facilitates the formation of long-chain hydrocarbons. In spite of the beneficial effects of MgO on the production of $C_{5+}$ hydrocarbons, the

transformation of MgO into inactive $MgCO_3$ during the $CO_2$ hydrogenation reaction results in the reoxidation of χ-$Fe_5C_2$ to iron-oxide phases and thus, a rapid decay in the $C_{5+}$ selectivity. The findings of this study, provide guidelines for the selection of a metal oxide promoter; if metal oxide promoters change their physicochemical properties during $CO_2$ hydrogenation, a more cautious approach is needed to understand the performance and stability of the bimetallic catalysts. In this context, the choice of metal oxide promotor that does not change its electronic states during the $CO_2$ conversion is highly crucial to develop a highly stable Fe-based catalyst.

## CRediT authorship contribution statement

**Sheraz Ahmed:** Conceptualization, Methodology, Formal analysis, Data curation, Witing − original draft. **Muhammad Irshad:** Methodology, Investigation, Data curation. **Wonjoong Yoon:** Validation, Formal analysis, Investigation. **Neha Karanwal:** Methodology, Formal analysis, Investigation. **Junjung Rohmat Sugiarto:** Conceptualization, Methodology, Investigation. **Muhammad Kashif Khan:** Conceptualization, Methodology, Formal analysis, Data curation. **Seok Ki Kim:** Conceptualization, Methodology, Investigation. **Jaehoon Kim:** Supervision, Project administration, Resources, Writing − review & editing, Funding acquisition.

## Declaration of Competing Interest

The authors declare that they have no known competing financial interests or personal relationships that could have appeared to influence the work reported in this paper.

## Data availability

Data will be made available on request.

## Acknowledgments

## Appendix A. Supporting information

Supplementary data associated with this article can be found in the online version at doi:10.1016/j.apcatb.2023.123052.

## References

[1] S.I. Seneviratne, M.G. Donat, A.J. Pitman, R. Knutti, R.L. Wilby, Allowable $CO_2$ emissions based on regional and impact-related climate targets, Nature 529 (2016) 477–483, https://doi.org/10.1038/nature16542.

[2] F. Kong, G. Rim, M. Song, C. Rosu, P. Priyadarshini, R.P. Lively, M.J. Realff, C. W. Jones, Research needs targeting direct air capture of carbon dioxide: Material & process performance characteristics under realistic environmental conditions, Korean J. Chem. Eng. 39 (2022) 1–19, https://doi.org/10.1007/s11814-021-0976-0.

[3] W.J. Wang, L. Scudiero, S. Ha, Recent progress in electrochemical reduction of $CO_2$ into formate and C2 compounds, Korean J. Chem. Eng. 39 (2022) 461–474, https://doi.org/10.1007/s11814-021-1009-8.

[4] W. Gao, S. Liang, R. Wang, Q. Jiang, Y. Zhang, Q. Zheng, B. Xie, C.Y. Toe, X. Zhu, J. Wang, L. Huang, Y. Gao, Z. Wang, C. Jo, Q. Wang, L. Wang, Y. Liu, B. Louis, J. Scott, A.-C. Roger, R. Amal, H. He, S.-E. Park, Industrial carbon dioxide capture

and utilization: state of the art and future challenges, Chem. Soc. Rev. 49 (2020) 8584–8686, https://doi.org/10.1039/D0CS00025F.

[5] J. Wei, R. Yao, Y. Han, Q. Ge, J. Sun, Towards the development of the emerging process of CO2 heterogenous hydrogenation into high-value unsaturated heavy hydrocarbons, Chem. Soc. Rev. 50 (2021) 10764–10805, https://doi.org/10.1039/D1CS00260K.

[6] R.-P. Ye, J. Ding, W. Gong, M.D. Argyle, Q. Zhong, Y. Wang, C.K. Russell, Z. Xu, A.G. Russell, Q. Li, M. Fan, Y.-G. Yao, CO2 hydrogenation to high-value products via heterogeneous catalysis, Nat. Commun. 10 (2019) 5698, https://doi.org/10.1038/s41467-019-13638-9.

[7] M.G. Sibi, D. Verma, H.C. Setiyadi, M.K. Khan, N. Karanwal, S.K. Kwak, K.Y. Chung, J.-H. Park, D. Han, K.-W. Nam, J. Kim, Synthesis of Monocarboxylic Acids via Direct CO2 Conversion over Ni–Zn Intermetallic Catalysts, ACS Catal. 11 (2021) 8382–8398, https://doi.org/10.1021/acscatal.1c00747.

[8] C.G. Visconti, M. Martinelli, L. Falbo, A. Infantes-Molina, L. Lietti, P. Forzatti, G. Iaquaniello, E. Palo, B. Picutti, F. Brignoli, CO2 hydrogenation to lower olefins on a high surface area K-promoted bulk Fe-catalyst, Appl. Catal. B: Environ. 200 (2017) 530–542, https://doi.org/10.1016/j.apcatb.2016.07.047.

[9] H. Jo, M.K. Khan, M. Irshad, M.W. Arshad, S.K. Kim, J. Kim, Unraveling the role of cobalt in the direct conversion of CO2 to high-yield liquid fuels and lube base oil, Appl. Catal. B: Environ. 305 (2022), 121041, https://doi.org/10.1016/j.apcatb.2021.121041.

[10] M.G. Sibi, M.K. Khan, D. Verma, W. Yoon, J. Kim, High-yield synthesis of BTEX over Na–FeAlOx/Zn–HZSM-5@ SiO2 by direct CO2 conversion and identification of surface intermediates, Appl. Catal. B: Environ. 301 (2022), 120813, https://doi.org/10.1016/j.apcatb.2021.120813.

[11] S.-M. Hwang, S.J. Han, H.-G. Park, H. Lee, K. An, K.-W. Jun, S.K. Kim, Atomically Alloyed Fe–Co Catalyst derived from a N-coordinated Co single-atom structure for CO2 hydrogenation, ACS Catal. 11 (2021) 2267–2278, https://doi.org/10.1021/acscatal.0c04358.

[12] M.K. Khan, P. Butolia, H. Jo, M. Irshad, D. Han, K.-W. Nam, J. Kim, Selective Conversion of Carbon Dioxide into Liquid Hydrocarbons and Long-Chain α-Olefins over Fe-Amorphous AlOx Bifunctional Catalysts, ACS Catal. 10 (2020) 10325–10338, https://doi.org/10.1021/acscatal.0c02611.

[13] B. Yao, T. Xiao, O.A. Makgae, X. Jie, S. Gonzalez-Cortes, S. Guan, A.I. Kirkland, J.R. Dilworth, H.A. Al-Megren, S.M. Alshihri, P.J. Dobson, G.P. Owen, J.M. Thomas, P.P. Edwards, Transforming carbon dioxide into jet fuel using an organic combustion-synthesized Fe-Mn-K catalyst, Nat. Commun. 11 (2020) 6395, https://doi.org/10.1038/s41467-020-20214-z.

[14] M.G. Sibi, D. Verma, J. Kim, Direct conversion of CO2 into aromatics over multifunctional heterogeneous catalysts, Catal. Rev. 64 (2022) 1–60, https://doi.org/10.1080/01614940.2022.2099058.

[15] C. Zhang, C. Cao, Y. Zhang, X. Liu, J. Xu, M. Zhu, W. Tu, Y.-F. Han, Unraveling the role of zinc on bimetallic Fe5C2–ZnO catalysts for highly selective carbon dioxide hydrogenation to high carbon α-olefins, ACS Catal. 11 (2021) 2121–2133, https://doi.org/10.1021/acscatal.0c04627.

[16] J. Wei, Q. Ge, R. Yao, Z. Wen, C. Fang, L. Guo, H. Xu, J. Sun, Directly converting CO2 into a gasoline fuel, Nat. Commun. 8 (2017) 15174, https://doi.org/10.1038/ncomms15174.

[17] J. Wei, J. Sun, Z. Wen, C. Fang, Q. Ge, H. Xu, New insights into the effect of sodium on Fe3O4-based nanocatalysts for CO2 hydrogenation to light olefins, Catal. Sci. Technol. 6 (2016) 4786–4793, https://doi.org/10.1039/C6CY00160B.

[18] N. Boreriboon, X. Jiang, C. Song, P. Prasassarakich, Fe-based bimetallic catalysts supported on TiO2 for selective CO2 hydrogenation to hydrocarbons, J. CO2 Util. 25 (2018) 330–337, https://doi.org/10.1016/j.jcou.2018.02.014.

[19] J. Zhu, G. Zhang, W. Li, X. Zhang, F. Ding, C. Song, X. Guo, Deconvolution of the particle size effect on CO2 hydrogenation over iron-based catalysts, ACS Catal. 10 (2020) 7424–7433, https://doi.org/10.1021/acscatal.0c01526.

[20] M.L. Luna, J. Timoshenko, D. Kordus, C. Rettenmaier, S.W. Chee, A.S. Hoffman, S.R. Bare, S. Shaikhutdinov, B.R. Cuenya, Role of the Oxide Support on the Structural and Chemical Evolution of Fe Catalysts during the Hydrogenation of CO2, ACS Catal. 11 (2021) 6175–6185, https://doi.org/10.1021/acscatal.1c01549.

[21] A. Noreen, M. Li, Y. Fu, C.C. Amoo, J. Wang, E. Maturura, C. Du, R. Yang, C. Xing, J. Sun, One-pass hydrogenation of CO2 to multibranched isoparaffins over bifunctional zeolite-based catalysts, ACS Catal. 10 (2020) 14186–14194, https://doi.org/10.1021/acscatal.0c03292.

[22] J. Wei, R. Yao, Q. Ge, Z. Wen, X. Ji, C. Fang, J. Zhang, H. Xu, J. Sun, Catalytic hydrogenation of CO2 to isoparaffins over Fe-based multifunctional catalysts, ACS Catal. 8 (2018) 9958–9967, https://doi.org/10.1021/acscatal.8b02267.

[23] Y. Ni, Z. Chen, Y. Fu, Y. Liu, W. Zhu, Z. Liu, Selective conversion of CO2 and H2 into aromatics, Nat. Commun. 9 (2018) 3457, https://doi.org/10.1038/s41467-018-05880-4.

[24] M.V. Cagnoli, S.G. Marchetti, N.G. Gallegos, A.M. Alvarez, R.C. Mercader, A.A. Yeramian, Influence of the support on the activity and selectivity of high dispersion Fe catalysts in the Fischer-Tropsch reaction, J. Catal. 123 (1990) 21–30, https://doi.org/10.1016/0021-9517(90)90154-C.

[25] M. Cagnoli, S. Marchetti, N.G. Gallegos, A.M. Alvarez, A.A. Yeramian, R.C. Mercader, Effect of thermal pretreatment on the structural properties of FeMgO catalysts in hydrocarbon synthesis from CO and H2, Mater. Chem. Phy 27 (1991) 403–418, https://doi.org/10.1016/0254-0584(91)90137-J.

[26] N. Gallegos, A.M. Alvarez, M.V. Cagnoli, J.F. Bengoa, S.G. Marchetti, R.C. Mercader, A.A. Yeramian, Selectivity to olefins of Fe/SiO2–MgO catalysts in the Fischer–Tropsch reaction, J. Catal. 161 (1996) 132–142, https://doi.org/10.1006/jcat.1996.0170.

[27] M. Luo, B.H. Davis, Fischer–Tropsch synthesis: Group II alkali-earth metal promoted catalysts, Appl. Catal. A: Gen. 246 (2003) 171–181, https://doi.org/10.1016/S0926-860X(03)00024-3.

[28] J. Yang, Y. Sun, Y. Tang, Y. Liu, H. Wang, L. Tian, H. Wang, Z. Zhang, H. Xiang, Y. Li, Effect of magnesium promoter on iron-based catalyst for Fischer–Tropsch synthesis, J. Mol. Catal. A: Chem. 245 (2006) 26–36, https://doi.org/10.1016/j.molcata.2005.08.051.

[29] A.N. Pour, S.M.K. Shahri, H.R. Bozorgzadeh, Y. Zamani, A. Tavasoli, M.A. Marvast, Effect of Mg, La and Ca promoters on the structure and catalytic behavior of iron-based catalysts in Fischer–Tropsch synthesis, Appl. Catal. A: Gen. 348 (2008) 201–208, https://doi.org/10.1016/j.apcata.2008.06.045.

[30] M. Arsalanfar, A.A. Mirzaei, H.R. Bozorgzadeh, A. Samimi, R. Ghobadi, Effect of support and promoter on the catalytic performance and structural properties of the Fe–Co–Mn catalysts for Fischer–Tropsch synthesis, J. Ind. Eng. Chem. 20 (2014) 1313–1323, https://doi.org/10.1016/j.jiec.2013.07.011.

[31] Y. Cheng, J. Lin, J. Tu, H. Wang, S. Xie, Y. Pei, S. Yan, M. Qiao, B. Zong, Mg and K dual-decorated Fe-on-reduced graphene oxide for selective catalyzing CO hydrogenation to light olefins with mitigated CO2 emission and enhanced activity, Appl. Catal. B: Environ. 204 (2017) 475–485, https://doi.org/10.1016/j.apcatb.2016.11.058.

[32] S.-Y. Li, L. Shuai, Y.-H. Zhang, J.-l Li, Z.-N. Liu, W. Li, Syngas-derived olefins over iron-based catalysts: Effects of basic properties of MgO nanocrystals, J. Fuel Chem. Technol. 46 (2018) 1342–1351, https://doi.org/10.1016/S1872-5813(18)30054-9.

[33] S. Badoga, G. Kamath, A. Dalai, Effects of promoters (Mn, Mg, Co and Ni) on the Fischer-Tropsch activity and selectivity of KCuFe/mesoporous-alumina catalyst, Appl. Catal. A: Gen. 607 (2020), 117861, https://doi.org/10.1016/j.apcata.2020.117861.

[34] Y. Wang, H.-X. Li, X.-G. Li, D. Chen, W.-D. Xiao, Effective iron catalysts supported on mixed MgO–Al2O3 for Fischer–Tropsch synthesis to olefins, Ind. Eng. Chem., Res. 59 (2020) 11462–11474, https://doi.org/10.1021/acs.iecr.0c01603.

[35] Z. Ma, W. Qian, H. Zhang, H. Ma, Q. Sun, W. Ying, High-temperature Fischer–Tropsch synthesis over the Li-promoted FeMnMgOx catalysts, Fuel 319 (2022), 123613, https://doi.org/10.1016/j.fuel.2022.123613.

[36] Y. Liu, X. Liu, Z. Yang, H. Li, X. Ding, M. Xu, X. Li, W.-F. Tu, M. Zhu, Y.-F. Han, Unravelling the metal–support interactions in χ-Fe5C2/MgO catalysts for olefin synthesis directly from syngas, Catal. Sci. Technol. 12 (2022) 762–772, https://doi.org/10.1039/D1CY02022F.

[37] J. Vaari, J. Lahtinen, A. Talo, P. Hautojärvi, Promotion of CO dissociation by magnesia on Co (0001), Surf. Sci. 251–252 (1991) 1096–1099, https://doi.org/10.1016/0039-6028(91)91157-S.

[38] J. Lahtinen, J. Vaari, A. Talo, A. Vehanen, P. Hautojärvi, Studies of Mg-O overlayers on Co (0001): growth mode and CO chemisorption properties, Surf. Sci. 245 (1991) 244–254, https://doi.org/10.1016/0039-6028(91)90027-P.

[39] J. Vaari, T. Vaara, J. Lahtinen, P. Hautojärvi, Adsorption of CO on Mg-promoted Co (poly), Appl. Surf. Sci. 81 (1994) 289–297, https://doi.org/10.1016/0169-4332(94)90286-0.

[40] M.K. Niemelä, A.O.I. Krause, Characterization of magnesium promoted Co/SiO2 catalysts, Catal. Lett. 34 (1995) 75–84, https://doi.org/10.1007/BF00808324.

[41] B. Ravel, M. Newville, ATHENA, ARTEMIS, HEPHAESTUS: data analysis for X-ray absorption spectroscopy using IFEFFIT, J. Synchrotron Rad. 12 (2005) 537–541, https://doi.org/10.1107/S0909049505012719.

[42] R.F. Susanti, L.W. Dianningrum, T. Yum, Y. Kim, B.G. Lee, J. Kim, High-yield hydrogen production from glucose by supercritical water gasification without added catalyst, Int. J. Hydrog. Energy 37 (2012) 11677–11690, https://doi.org/10.1016/j.ijhydene.2012.05.087.

[43] S.J. Clark, M.D. Segall, C.J. Pickard, P.J. Hasnip, M.I.J. Probert, K. Refson, M.C. Payne, First principles methods using CASTEP, Z. Kryst. 220 (2005) 567–570, https://doi.org/10.1524/zkri.220.5.567.65075.

[44] J.P. Perdew, K. Burke, M. Ernzerhof, Generalized gradient approximation made simple, Phys. Rev. Lett. 77 (1996) 3865–3868, https://doi.org/10.1103/PhysRevLett.77.3865.

[45] D.J. Chadi, Special points for Brillouin-Zone integrations, Phys. Rev. B 16 (1977) 5188–5192, https://doi.org/10.1103/PhysRevB.16.1746.

[46] G. Liu, S. Ji, L. Yin, G. Fei, C. Ye, An investigation of the electronic properties of MgO doped with group III, IV, and V elements: trends with varying dopant atomic number, J. Phys.: Condens. Matter 22 (2010) 4, https://doi.org/10.1088/0953-8984/22/4/046002.

[47] D. Sanchez-Portal, E. Artacho, J.M. Soler, Projection of plane-wave calculations into atomic orbitals, Solid State Commun. 95 (1995) 685–690, https://doi.org/10.1016/0038-1098(95)00341-X.

[48] J. Zhu, P. Wang, X. Zhang, G. Zhang, R. Li, W. Li, T.P. Senftle, W. Liu, J. Wang, Y. Wang, A. Zhang, Dynamic structural evolution of iron catalysts involving competitive oxidation and carburization during CO2 hydrogenation, Sci. Adv. 8 (2022), https://doi.org/10.1126/sciadv.abm3629.

[49] N. McQueen, P. Kelemen, G. Dipple, P. Renforth, J. Wilcox, Ambient weathering of magnesium oxide for CO2 removal from air, Nat. Commun. 11 (2020) 3299, https://doi.org/10.1038/s41467-020-16510-3.

[50] L. Tang, L. He, Y. Wang, B. Chen, W. Xu, X. Duan, A.-H. Lu, Selective fabrication of χ-Fe5C2 by interfering surface reactions as a highly efficient and stable Fischer-Tropsch synthesis catalyst, Appl. Catal. B: Environ. 284 (2021), 119753, https://doi.org/10.1016/j.apcatb.2020.119753.

[51] E. de Smit, B.M. Weckhuysen, The renaissance of iron-based Fischer-Tropsch synthesis: on the multifaceted catalyst deactivation behavior, Chem. Soc. Rev. 37 (2008) 2758–2781, https://doi.org/10.1039/B805427D.

[52] X. Zhou, G.J.A. Mannie, J. Yin, X. Yu, C.J. Weststrate, X. Wen, K. Wu, Y. Yang, Y. Li, J.W. Niemantsverdriet, Iron carbidization on thin-film silica and silicon: A near-ambient-pressure X-ray photoelectron spectroscopy and scanning tunnling microscopy study, ACS Catal. 8 (2018) 7326–7333, https://doi.org/10.1021/acscatal.8b02076.

[53] L.L. Skovbjerg, D.V. Okhrimenko, J. Khoo, K.N. Dalby, T. Hassenkam, E. Makovicky, S.L.S. Stipp, Preferential adsorption of hydrocarbons to nanometer-sized clay on chalk particle surfaces, Energy Fuels 27 (2013) 3642–3652, https://doi.org/10.1021/ef301832b.

[54] W. Wang, Y. Liu, Y. Yue, H. Wang, G. Cheng, C. Gao, C. Chen, Y. Ai, Z. Chen, X. Wang, The confined interlayer growth of ultrathin two-dimensional $Fe_3O_4$ nanosheets with enriched oxygen vacancies for peroxymonosulfate activation, ACS Catal. 11 (2021) 11256–11265, https://doi.org/10.1021/acscatal.1c03331.

[55] M. Amoyal, R. Vidruk-Nehemya, M.V. Landau, M. Herskowitz, Effect of potassium on the active phases of Fe catalysts for carbon dioxide conversion to liquid fuels through hydrogenation, J. Cat. 348 (2017) 29–39, https://doi.org/10.1016/j.jcat.2017.01.020.

[56] N.S. McIntyre, D.G. Zetaruk, X-ray photoelectron spectroscopic studies of iron oxides, Anal. Chem. 49 (1977) 1521–1529, https://doi.org/10.1021/ac50019a016.

[57] M.C. Biesinger, B.P. Payne, A.P. Grosvenor, L.W.M. Lau, A.R. Gerson, R.S.C. Smart, Resolving surface chemical states in XPS analysis of first row transition metals, oxides and hydroxides: Cr, Mn, Fe, Co and Ni, Appl. Surf. Sci. 257 (2011) 2717–2730, https://doi.org/10.1016/j.apsusc.2010.10.051.

[58] M. Santamaria, F.D. Quarto, S. Zanna, P. Marcus, Initial surface film on magnesium metal: A characterization by X-ray photoelectron spectroscopy (XPS) and photocurrent spectroscopy, Electrochim. Acta 53 (2007) 1314–1324, https://doi.org/10.1016/j.electacta.2007.03.019.

[59] M. Kumar, F. Aberuagba, J.K. Gupta, K.S. Rawat, L.D. Sharma, G.M. Dhar, Temperature-programmed reduction and acidic properties of molybdenum supported on MgO-$Al_2O_3$ and their correlation with catalytic activity, J. Mol. Catal. A: Chem. 213 (2004) 217–223, https://doi.org/10.1016/j.molcata.2003.12.005.

[60] J. Zielinski, I. Zglinicka, L. Znak, Z. Kaszkur, Reduction of $Fe_2O_3$ with hydrogen, Appl. Catal. A: Gen. 381 (2010) 191–196, https://doi.org/10.1016/j.apcata.2010.04.003.

[61] F. Bozso, G. Ertl, M. Grunze, M. Weiss, Chemisorption of hydrogen on iron surface, Appl. Surf. Sci. 1 (1977) 103–119, https://doi.org/10.1016/0378-5963(77)90009-5.

[62] H. Sun, S. Wang, C. Zhang, J. Xu, B. Wu, Y. Yang, H. Xiang, Y.-W. Li, Chemical and structural effects of silica in iron-based Fischer-Tropsch synthesis catalysts, J. Catal. 286 (2012) 111–123, https://doi.org/10.1016/j.jcat.2011.10.024.

[63] J. Harris, S. Andersson, $H_2$ dissociation at metal surfaces, Phys. Rev. Lett. 55 (1985) 1583–1586, https://doi.org/10.1103/PhysRevLett.55.1583.

[64] J.I.D. Cosimo, V.K. Diez, M. Xu, E. Iglesia, C.R. Apesteguia, Structure and surface and catalytic properties of Mg-Al basic oxides, J. Catal. 178 (1998) 499–510, https://doi.org/10.1006/jcat.1998.2161.

[65] J.I.D. Cosimo, C.R. Apesteguia, M.J.L. Gines, E. Iglesia, Structural requirements and reaction pathways in condensation reactions of alcohols on $MgyAlO_x$ catalysts, J. Catal. 190 (2000) 261–275, https://doi.org/10.1006/jcat.1999.2734.